AIMS Mathematics, 10(4): 10093–10123.
DOI: 10.3934/math.2025460
Received: 18 January 2025
Revised: 26 March 2025
Accepted: 03 April 2025
Published: 28 April 2025

http://www.aimspress.com/journal/Math

Research article

Utilizing the Box-Behnken method on modeling of ternary-Casson nanofluid with variable density and heat sink across a vertical jet

Umar Nazir[1] and Abdelaziz Nasr[2,*]

[1] Department of Mathematics, Faculty of Science, Khon Kaen University, Khon Kaen 40002, Thailand
[2] Mechanical Engineering Department, College of Engineering and Architecture, Umm Al-Qura University, P.O. Box 5555, Makkah 21955, Saudi Arabia

* **Correspondence:** Email: ahnasr@uqu.edu.sa.

Abstract: In this paper, the thermal performance of Casson fluid is discussed with variable density while the vertical jet is taken out. The correlation of tri-hybrid nanofluid was utilized whereas base fluid was addressed as ethylene glycol, and suspension of CuO, GO and aluminum oxide were considered because of their superior heat transfer capabilities, such as electronic cooling and heat exchangers. For increased energy efficiency, these nanofluids were also utilized in industrial cooling systems, solar collectors, and automobile radiators. Darcy's law was used with heat sink and viscous dissipation. The development of the mathematical model was visualized in terms of PDEs. The finite element method was used for numerical procedures. The novel aspect included using the Box-Behnken design for optimization and the finite element method to analyze tri-hybrid nanofluid flow over a vertical jet with Darcy-Forchheimer effects, heat source, and viscous dissipation. It was claimed that highly novelty work is discussed. The Box Behnken design was employed for calculating Nusselt number and divergent velocity. We concluded that the motion of nanofluid is enhanced when Forchiermer number and B are enhanced. The temperature profile is boosted when heat sink and Eckert number, D , and the power law index number are enhanced. Ternary hybrid nano-fluid has remarkable achievement in heat transfer rate and divergent velocity than hybrid nanofluid and nanofluid.

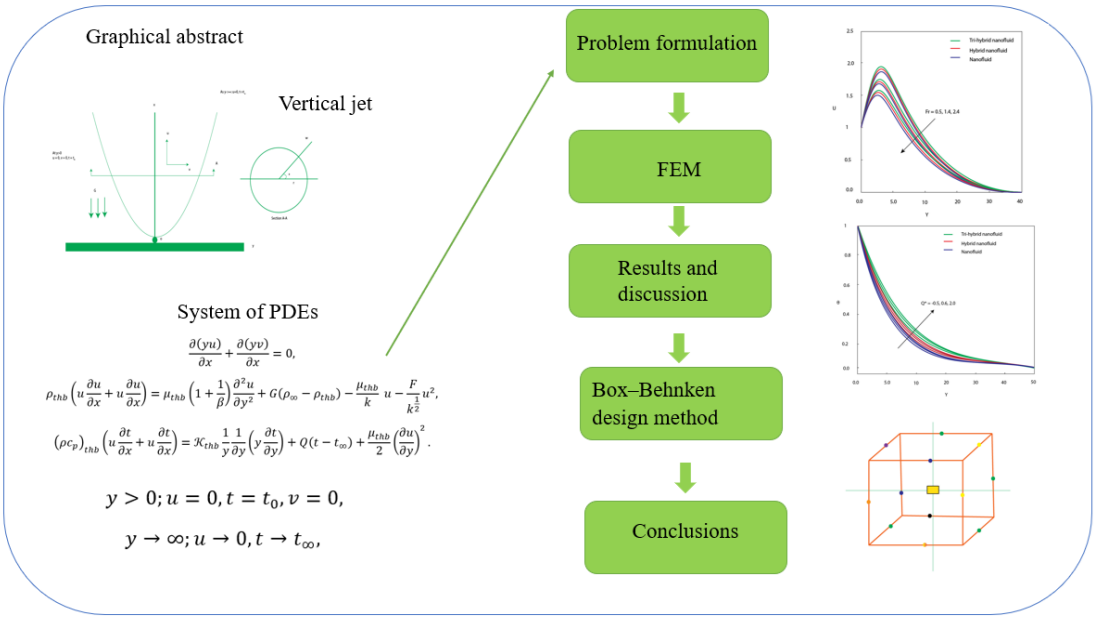

Keywords: tri-hybrid nanofluid; Box–Behnken design; vertical jet; Darcy's Forchhiermer law; heat sink; finite element method

Nomenclature:

u, v	Velocity components(m/s)	y, x	Space coordinates (m)
ρ	Fluid density (kg/m³)	μ	Viscosity (kg/(m·s)
k	Permeability of the medium (m²)	F	External force parameter (N/m³)
π_c	Casson number (−)	ρ_∞	Free stream density (kg/m³)
G	Gravitational acceleration (m/s²)	$\mathcal{K}$	Thermal conductivity (W/m·K)
c_p	Specific heat capacitance (J/kg·K)	Q	Heat sink (W/m³)
T	Dimensionless temperature	∞	Infinity (−)
t_0	Reference temperature	t_∞	Ambient temperature
Ẍ, Ÿ	Space coordinates (m)	β	Casson number (−)
ODEs	Ordinary differential equations (−)	ν	Viscosity (m²/s)
ϵ	Darcy's number (−)	Fr	Forchhiermer number (−)
Pr	Prandtl number (−)	Ec	Eckert number (−)
Q^*	Heat source number (−)	N_1, N_1, N_3	Volume fractions (−)
Al_2O_3	Aluminum oxide (−)	CuO	Copper oxide (−)
GO	Graphene Oxide (−)	Cf	Skin friction coefficient (−)
Nu	Nusselt number (−)	Re	Reynolds number (−)
t	Temperature (K)	D	Fluid absorption number (−)
Ec	Eckert number (−)	thb	Tri-hybrid nanofluid (−)
f	Base fluid (−)	hb	Hybrid nanofluid (−)
nf	Nanofluid (−)	FEM	Finite element method (−)
m	Density parameter (−)	Ü, V̈	Velocity components (m/s)
β^*	Volumetric expansion coefficient (K^{-1})	THNF	Tri-hybrid nanofluid

1. Introduction

The suspension of ternary hybrid nanofluid is composed of three kinds of nanoparticles suspended in a base fluid (such as ethylene glycol) to improve its viscosity, thermal conductivity, and other thermophysical characteristics. These fluids are extensively researched in heat transfer applications, such as renewable energy systems, cooling systems, and biomedical applications. A finite element scheme is used to analyze the fluid flow, heat transfer, and other properties of ternary hybrid nanofluids. FEM is especially helpful for resolving non-linear problems and complex geometries. Sohail et al. [1] investigated the results of tetra-hybrid nanofluid towards a vertical disk. The induced magnetic field was utilized. They used non-Fourier's law and thermal radiation (non-linear). The numerical results have been done by finite element scheme. Shamshuddin et al. [2] used the HAM method to study a rotating disk system with tri-hybrid nanoparticles being affected by magnetic fields, viscous dissipation, and Hall currents. According to the results, tri-hybrid nanofluids have better velocity profiles than single (Cu) and hybrid (Cu-FeO_4) nanofluids. By adding nanoparticles, the base fluid's energy transfer efficiency is greatly increased. Shamshuddin et al. [3] studied the HAM to investigate how different chemical reactions affect the flow of hybrid nanofluids that incorporate Prandtl nanoparticles and Ohmic heating. Results show that lowering molecular diffusivity by increasing the chemical reaction parameter results in a decrease in concentration field profiles. This demonstrated that the interaction between reaction dynamics and fluid behavior is enhanced by nanoparticles. Shamshuddin et al. [4] worked on ternary hybrid nanofluids, like MWCNT-Au-Ag/blood mixtures. They included that THNF has various applications like atomic reactors, solar energy systems, heat pipes, cars, and biomedical engineering. The flow of such nanofluids over a bidirectional stretching sheet is investigated in this work, which is motivated by developments in nanotechnology. Ali et al. [5] focused on heat radiation and Soret effects over an inclined stretching sheet, this work explored nanofluid flow within a micropolar MHD framework. The LMB optimization technique is used to solve the governing ODEs. The analysis emphasizes how thermal and concentration gradients interact in sophisticated fluid mechanics. Khan et al. [6] studied on neural network-based optimization technique called the Levenberg–Marquardt (LM) backpropagation algorithm to numerically assess electromagnetohydrodynamic bioconvection in micropolar nanofluids. To analyze the flow behavior, the study takes into account stratification effects and thermal radiation. The method has described how effective sophisticated computational methods are in complex fluid dynamics. Alqahtani et al. [7] discussed energy enhancement in THB Carreau Yasuda nanofluid flow with a magnetic dipole across a vertical sheet. The fluid, was enriched with MWCNTs, Zn, and Cu in ethylene glycol using activation energy, heat source/sink, chemical reactions, and Darcy-Forchheimer effects. Practical effects like Joule heating and a magnetic field are incorporated into the flow analysis by Rahman et al. [8]. This investigates a hybrid nanofluid's two-dimensional flow in a porous medium enclosed by two parallel walls. Jan et al. [9] discussed the study of thermal radiation with a cross-model ternary hybrid nanofluid's laminar flow. The flow takes place in a porous medium under a magnetic field and is impacted by a stretching cylinder. Rahman et al. [10] examined Darcy-Brinkman flow across a stretched sheet while taking frictional heating and porous dissipation into account. The RK4 method was used to analyze the steady flow of a dusty fluid through a porous medium while accounting for slip effects. Rehman et al. [11] explored Darcy-Forchheimer flow across a porous curved stretching surface. To account for high-velocity effects in porous media, the model integrates Darcy's law with Forchheimer corrections. The governing equations are solved using HAM. Khan et al. [12] investigated

chemically reactive exothermic fluid flow through a porous medium under gravity with MHD. The modified Darcy law was used to model the resistance of the porous medium. To solve the equations, a semi-implicit (FDA) has been used. Hayat et al. [13] estimated the peristaltic flow of MHD hybrid nanofluids in a symmetric channel. The Darcy–Forchheimer law is used to analyze the nonlinear behavior of porous media. They examined the effects of viscous dissipation and Joule heating. Adun et al. [14] studied a novel ternary hybrid nanofluid's thermophysical characteristics for use in energy applications. Its performance was optimized through experimental techniques. The results were intended to increase practical systems' energy efficiency. Lone et al. [15] utilized bvp4c method to solve the transformed equations. The ternary nanofluid's thermal efficiency can be increased by several factors, including thermophoresis, thermal radiation, Biot number, Eckert number, and magnetic field. The performance of heat transfer was greatly influenced by these factors. Khan et al. [16] examined the flow of ternary hybrid nanofluids over a stretching surface while considering porosity, magnetic effects, heat generation, and viscous dissipation. The ANN approach was used in a machine learning approach. Tanuja et al. [17] experienced the LTNE model used to investigate heat transfer in wetted rectangular porous fins. The Darcy model and Boussinesq approximation were used to analyze buoyancy with forces, and convection and radiation effects. It was estimated that the temperature profiles of the solid and ternary nanofluid phases were improved by lowering the surface-ambient radiation parameter. This suggests that heat transfer performance has been improved. Kim et al. [18] determined that heat transfer and magnetohydrodynamic natural convection in a ternary-hybrid nanofluid inside a partially heated porous square cavity are the main topics of this work. Additionally, the effects of thermal radiation and heat generation and absorption were examined. Mohanty et al. [19] estimated a cross-ternary hybrid nanofluid containing the nanoparticles SWCNT, MWCNT, and GO around a vertical cylinder. The thermophysical behavior of the nanoparticles was highlighted by the significant influence of Joule heating and radiation on thermal performance. Entropy generation is examined using the HAM. Ullah et al. [20] examined the thermal behavior of tri-hybrid nanofluid flow over an expanding disk, incorporating nanoparticles in a water-based solution. They investigate heat transfer and fluid dynamics under the influence of quadratic convection, ohmic heating, and a magnetic field. HAM is used to provide insights into enhanced thermal performance. Mohanty et al. [21] experienced the study of tri-hybrid nano-particles on a rotating disk with statistical analysis. They employed a finite element scheme for numerical outcomes. They also included that platelet-shaped nanofluid was more significant than other shapes of nanofluid for the case of heat transfer purposes. Faizan et al. [22] studied the mechanism of ternary hybrid nanofluid on the surface including Williamson fluid. They estimated entropy generation with thermal radiation and heat sink with convective boundary conditions. Ramzan et al. [23] discussed the role of Carreau fluid in multiple nanoscales under the influence of MHD with entropy generation. They estimated that maximum heat energy using ternary hybrid nano-fluid. Mishra et al. [24] discussed the novelty work of the machine learning approach on heat transfer inclusion of tri-hybrid nanofluid. They took three geometries considering heat sink, non-Fourier's law, and thermal radiation. They utilized bvp4c. Mishra [25] studied waste discharge with the hybrid nanofluid on a stretching/shrinking surface utilizing a chemical reaction. Mishra has worked on Darcy's law using the bvp4c approach. Mishra included that concentration profiles enhance with increment of unsteadiness parameter. Mishra [26] observed the significant role of hybrid nanofluid with base fluids (ethylene glycol and water) on a permeable plate. Thompson and Troian slip influences were considered. The numerical results have been obtained using the bvp4c approach. Mishra [27] discussed the study of gyrotactic microorganisms with Xue and

Yamada-Ota models on an exponential sheet. Brownian motion, viscous dissipation, and radiation parameters are considered. Ramasekhar et al. [28] utilized a hybrid nanofluid in Casson fluid with a heat source and thermal radiation (non-linear). An approach called bvp5c has been utilized for numerical purposes. Basha et al. [29] discussed the characterizations of Casson fluid with thermal radiation. The numerical consequences have been attained using OHAM. Chabani and Mebarek-Oudina [30] estimated the role of a hybrid nanofluid utilizing a finite element approach. Mezaache et al. [31] visualized thermal energy in a heat exchanger channel. They discussed the influence of entropy generation. They studied Darcy–Forchheimer law in nanofluid with a thermal equilibrium approach.

The Xue model is frequently used to predict the effective thermal conductivity of nanofluids that contain cylindrical nanoparticles. However, applications of the Xue model can be extended to various nanoparticles based on CuO, graphene oxide and Al_2O_3 in ethylene glycol. The thermal conductivity of CuO and Al_2O_3 nanoparticles dissolved in ethylene glycol was examined in a study [32]. Sundar et al. [32] showed that both kinds of nanoparticles improved the base fluid's thermal conductivity, confirming the predictive value of models such as Xue's. Zhang et al. [33] studied the Xue and Maxwell models for hybrid nanofluids. They showed that the Xue model can be applied to different nanoparticle compositions and shapes, such as CuO and Al_2O_3. Zhang et al. [34] discussed the application of the Xue model to predict the thermal behavior of nanofluids containing ethylene glycol as the base fluid. They observed that the Xue model has been effectively used to evaluate thermal conductivity in studies involving the peristaltic flow of hybrid nanofluids based on ethylene glycol. Tri-hybrid nanofluid is the suspension of three nanofluids in base fluid (ethylene glycol). Tri-hybrid nanofluid has the ability of heat transfer in comparison to base fluids like ethylene glycol, oil and water, etc. The various models of Xue, Yamada-Ota, and Hamilton-Crosser are studied for heat transfer enhancement. The Yamada Ota-model is used for predicting the volume fractions and particle size due to thermal conductivity. Xue model is called the two-phase model that is utilized in such processes where heat transfers in the solid phase and fluid phase. Both models have been used in cooling systems, solar thermal collectors, engine cooling fluids, drug delivery processes, photovoltaic cooling, and HVAC systems. Galal et al. [35] discussed the models (Xue and Yamada Ota) in Casson fluid considering various nanofluid over-stretching 3D surfaces via local thermal (non-equilibrium). Rafiq et al. [36] discussed comparison analysis between Yamad Ota and Xue, including hybrid nanofluid on disk via Lorentz force.

Heat exchangers, nuclear power plants, jet engine cooling, electronic cooling, solar energy systems, drug delivery systems, and metal cutting/machining fluids are the applications of ternary hybrid nanofluids that are depicted in Figure 1.

Table 1 describes the comparative novelty analysis with published works [37–40]. It is noticed that tri-hybrid nanofluid, Darcy-Forchheimer law, heat source, and viscous dissipation on a vertical jet are not studied in the current model. Further, the finite element approach is used while the Box–Behnken design is utilized. It is claimed that novelty work is discussed in the section on the formulation of the problem. Applications for the study of tri-hybrid nanofluids in a vertical jet using the finite element method and Darcy-Forchheimer law include industrial heat exchangers, thermal energy storage, and sophisticated cooling systems. The Box-Behnken design enhances heat transfer efficiency, supporting microfluidic devices, biomedical cooling, and aerospace propulsion.

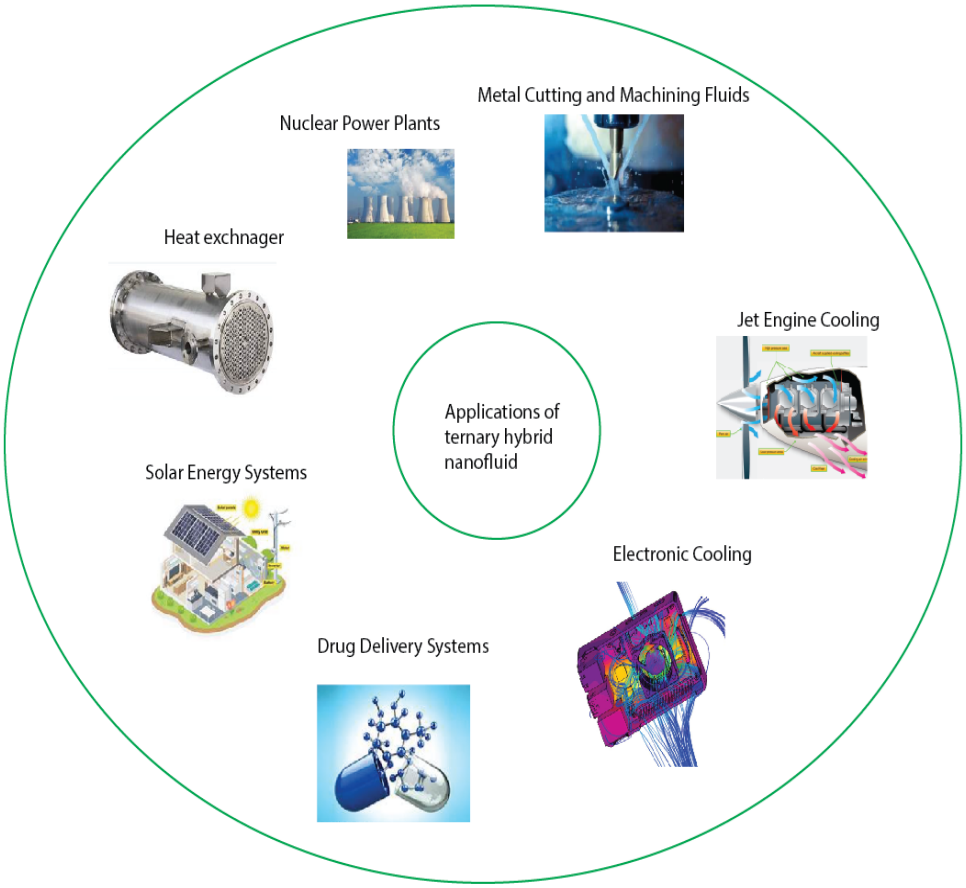

Figure 1. Applications of tri-hybrid nanofluid.

Table 1. Novelty work of current model.

Authors	Vertical jet	Darcy-Forchheimer law	Heat source	Viscous dissipation	Finite element method
Maryam et al. [37]	✓	X	X	X	X
Mollendorf and Gebhart [38]	✓	X	X	X	X
Mogi et al. [39]	✓	X	X	X	X
Siddiqa et al. [40]	✓	X	X	X	X

2. Modeling of the problems

A 2D flow of Casson fluid with steady motion is considered on an oriented round jet along with axial symmetry. The coordinate system is in line with the direction normal to the jet and the axis of symmetry. Except for density, which drops exponentially with temperature, the fluid's characteristics are constant and it is incompressible. It is assumed that the centerline temperature is much higher than the fluid's ambient temperature. The effects of Casson fluid behavior and tri-hybrid nanofluid flow are considered. The Darcy-Forchheimer law, which takes into consideration the resistance of porous

media, controls the jet's flow. To simulate energy dissipation, a heat sink is incorporated. The geometry is described in Figure 2. It is noticed that ethylene glycol is discovered as a non-Newtonian [41] and shear thinning [42]. The rheology of Casson fluid is non-Newtonian. Therefore, a combined study of Casson fluid with ethylene glycol is discussed in this model since such phenomena are used in energy-efficient thermal transport, biomedical fluids, and cooling systems. Thus, due to its superior thermal qualities such as its high thermal conductivity, low freezing point, and chemical stability, ethylene glycol is selected as the base fluid for heat transfer applications.

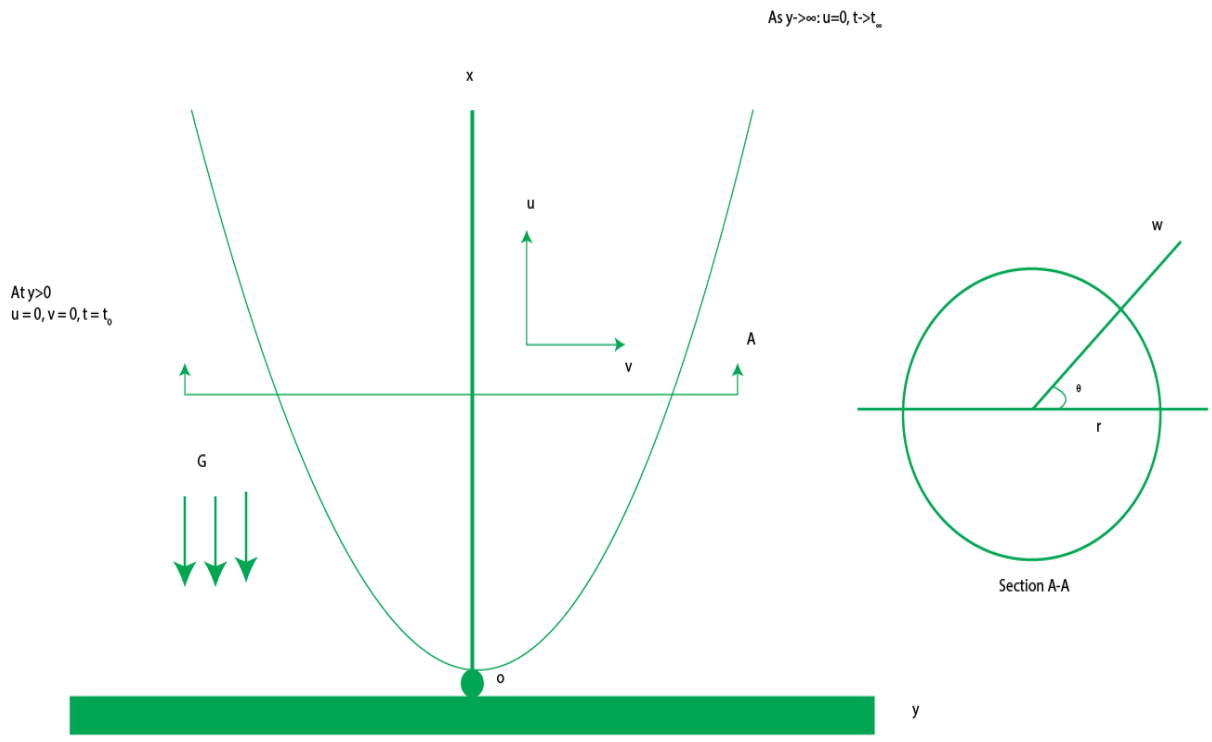

Figure 2. Geometry of the model.

Figure 2 describes the diagram of a vertical jet, and the coordinate system is adjusted as the x-axis is taken as a normal direction while the y-axis is taken as a horizontal direction. The motion of the nanofluid on a vertical jet is produced using wall velocity. It is noticed that velocity components u are along the y-axis and v is taken along the x-axis. The flow is influenced by gravity (G). A cross-section area is denoted by tangential velocity w. The ambient temperature is assumed as t_∞. The centerline temperature of the jet is much higher than the ambient fluid temperature t_∞, resulting in a thermal gradient that affects fluid motion and heat transfer as the jet expands vertically. Applications of vertical jets are cooling systems and fuel injection. It improves cooling in gas turbines, electronics, and material processing by causing a high-velocity jet to strike a surface. Optimizing industrial spraying, biomedical drug delivery, and propulsion systems through an understanding of velocity, pressure, and thermal boundary layers in such jets enhances performance and efficiency in engineering applications. The

following assumptions are listed below.

- A steady flow of Casson fluid is considered;
- A vertical jet is used;
- Darcy's and Forchhiermer's law are discussed;
- An incompressible and two-dimensional flow are considered;
- Viscous dissipation and heat sink are utilized;
- Variable thermal conductivity is used;
- Xue and Yamada Ota hybrid nanofluid are inserted.

A nonlinear rheological model known as the Casson fluid model explains how viscoelastic fluids behave when they experience yield stress. The stress tensor of Casson fluid [43] is defined as

$$\boldsymbol{\tau} = \left[\mu + \left(\frac{P_y}{(2\pi_e)^{\frac{1}{2}}}\right)^{\frac{1}{n}}\right]^n, \tag{1}$$

In Eq (1), π_e is formulated using a component of deformation rate, π_e is called critical value, μ is termed as plastic dynamic viscosity and P_y is called yield stress. It is noticed that the stress tensor of Casson fluid for $n = 1$ is defined [43] as

$$\boldsymbol{\tau} = \left[\mu + \frac{P_y}{(2\pi_e)^{\frac{1}{2}}}\right]\boldsymbol{A}. \tag{2}$$

Here, A is known as the Rivlin-Ericksen tensor. It is noted that Eq (2) can be reduced into Casson fluid when $P_y = 0$. The model of PDEs [37-40] is defined as

$$\frac{\partial(yu)}{\partial x} + \frac{\partial(yv)}{\partial x} = 0, \tag{3}$$

$$\rho_{thb}\left(u\frac{\partial u}{\partial x} + u\frac{\partial u}{\partial x}\right) = \mu_{thb}\left(1 + \frac{1}{\beta}\right)\frac{\partial^2 u}{\partial y^2} + G(\rho_\infty - \rho_{thb}) - \frac{\mu_{thb}}{k}\,u - \frac{F}{k^{\frac{1}{2}}}u^2, \tag{4}$$

$$\left(\rho c_p\right)_{thb}\left(u\frac{\partial t}{\partial x} + u\frac{\partial t}{\partial x}\right) = \mathcal{K}_{thb}\frac{1}{y}\frac{1}{\partial y}\left(y\frac{\partial t}{\partial y}\right) + Q(t - t_\infty) + \frac{\mu_{thb}}{2}\left(1 + \frac{1}{\beta}\right)\left(\frac{\partial u}{\partial y}\right)^2. \tag{5}$$

Equation (3) describe continuity equation for the case of steady and incompressible flow. Equation (4) describes the momentum equation in the presence of Casson fluid. The term related to $u\frac{\partial u}{\partial x} + u\frac{\partial u}{\partial x}$ is called convective acceleration, $\mu_{thb}\left(1 + \frac{1}{\beta}\right)\frac{\partial^2 u}{\partial y^2}$ is viscous dissipation in the presence of Casson fluid, $G(\rho_\infty - \rho_{thb})$ reveals the buoyancy force because of density variations, $-\frac{\mu_{thb}}{k}\,u - \frac{F}{k^{\frac{1}{2}}}u^2$ are formulated due to Darcy's Forchhiermer law. Equation (5) is called energy equation, $\left(u\frac{\partial t}{\partial x} + u\frac{\partial t}{\partial x}\right)$ is convective heat, $\mathcal{K}_{thb}\frac{1}{y}\frac{1}{\partial y}\left(y\frac{\partial t}{\partial y}\right)$ is diffusion of heat due variable thermal

conductivity, $Q(t-t_\infty)$ is the heat source and $\frac{\mu_{thb}}{2}\left(\frac{\partial u}{\partial y}\right)^2$ is the viscous dissipation term.

BCs [37] are defined as

$$y>0; u=0, t=t_0, v=0,$$

$$y\to\infty; u\to 0, t\to t_\infty, \tag{6}$$

Now, dimensionless parameters are defined [37] as

$$\ddot{X}=x\left(\frac{G\beta\Delta t_0}{\nu_f^2}\right)^{1/3}, \ddot{Y}=y\left(\frac{G\beta\Delta t_0}{\nu_f^2}\right)^{1/3}, \ddot{V}=\frac{v}{\left(\nu_f G\beta\Delta t_0\right)^{\frac{1}{3}}}, T=\frac{t-t_\infty}{t_0-t_\infty}, \tag{7}$$

$$\ddot{U}=\frac{u}{\left(\nu_f G\beta\Delta t_0\right)^{\frac{1}{3}}}, \Delta t_0=t-t_\infty,$$

Dimensionless ODEs [37] are

$$\frac{\partial\left(\ddot{Y}\,\ddot{U}\right)}{\partial\ddot{X}}+\frac{\partial\left(\ddot{Y}\,\ddot{V}\right)}{\partial\ddot{Y}}=0, \tag{8}$$

$$\frac{\nu_f}{\nu_{thb}}\left(\ddot{U}\frac{\partial\ddot{U}}{\partial\ddot{X}}+\ddot{V}\frac{\partial\ddot{U}}{\partial\ddot{Y}}\right)=\left(1+\frac{1}{\beta}\right)\frac{\partial^2\ddot{U}}{\partial\ddot{Y}^2}e^{mT}+\frac{\nu_f}{\nu_{thb}}e^{mT}T-\epsilon\,\ddot{U}-\frac{\nu_f}{\nu_{thb}}Fr\ddot{U}^2, \tag{9}$$

$$\frac{\mathcal{K}_f}{\mathcal{K}_{thb}}\frac{\left(\rho c_p\right)_{thb}}{\left(\rho c_p\right)_f}\left(\ddot{U}\frac{\partial(T)}{\partial\ddot{X}}+\ddot{V}\frac{\partial(T)}{\partial\ddot{X}}\right)=\frac{e^{mT}}{Pr}\left[\frac{1}{\ddot{Y}}\frac{\partial}{\partial\ddot{Y}}\left(\ddot{Y}\frac{\partial T}{\partial\ddot{Y}}\right)\right]+\left(1+\frac{1}{\beta}\right)\frac{\mathcal{K}_f}{\mathcal{K}_{thb}}\frac{\left(\rho c_p\right)_{thb}}{\left(\rho c_p\right)_f}\frac{Ec}{2Pr}\left(\frac{\partial\ddot{U}}{\partial\ddot{Y}}\right)^2 + \frac{\mathcal{K}_f}{Pr\mathcal{K}_{thb}}Q^*T. \tag{10}$$

Dimensionless BCs [37] are

$$\ddot{Y}>0; T=1, \ddot{U}=0, \ddot{V}=0,$$

$$\ddot{Y}\to 0; T\to 0, \ddot{U}\to 0, \tag{11}$$

The model for the ternary hybrid nanofluid [42] is provided as

$$\frac{\mu_f}{(1-N_3)^{2.5}(1-N_2)^{2.5}(1-N_1)^{2.5}}=\mu_{thb}, \tag{12}$$

$$\rho_{thb}=(1-N_1)\left\{(1-N_2)\left[(1-N_3)\rho_f+N_3\rho_3\right]+N_2\rho_2\right\}+N_1\rho_1, \tag{13}$$

$$\frac{\mathcal{K}_{hb}}{\mathcal{K}_{nf}}=\frac{\mathcal{K}_2+2\mathcal{K}_{nf}-2N_2\left(\mathcal{K}_{nf}-\mathcal{K}_2\right)}{\mathcal{K}_2+2\mathcal{K}_{nf}+N_2\left(\mathcal{K}_{nf}-\mathcal{K}_2\right)},\frac{\mathcal{K}_{thb}}{\mathcal{K}_{hb}}=\frac{\mathcal{K}_3+2\mathcal{K}_{hb}-2N_3(\mathcal{K}_{hb}-\mathcal{K}_3)}{\mathcal{K}_3+2\mathcal{K}_{hb}+N_3(\mathcal{K}_{hb}-\mathcal{K}_3)}, \tag{14}$$

$$\frac{\mathcal{K}_{nf}}{\mathcal{K}_f}=\frac{\mathcal{K}_1+2\mathcal{K}_f-2N_1\left(\mathcal{K}_f-\mathcal{K}_1\right)}{\mathcal{K}_1+2\mathcal{K}_f+N_1\left(\mathcal{K}_f-\mathcal{K}_1\right)},\frac{\sigma_{nf}}{\sigma_f}=\frac{\sigma_1+2\sigma_f-2N_1\left(\sigma_f-\sigma_1\right)}{\sigma_1+2\sigma_f+N_1\left(\sigma_f-\sigma_1\right)}, \tag{15}$$

$$\frac{\sigma_{thb}}{\sigma_{hb}}=\frac{\sigma_3+2\sigma_{hb}-2N_3(\sigma_{hb}-\sigma_3)}{\sigma_3+2\sigma_{hb}+N_3(\sigma_{hb}-\sigma_3)},\frac{\sigma_{hb}}{\sigma_{nf}}=\frac{\sigma_2+2\sigma_{nf}-2N_2\left(\sigma_{nf}-\sigma_2\right)}{\sigma_2+2\sigma_{nf}+N_2\left(\sigma_{nf}-\sigma_2\right)}. \tag{16}$$

The ternary hybrid Xue model [44] is described as

$$\frac{\mathcal{K}_{Thb}}{\mathcal{K}_{nf}}=\frac{1-N_3+2N_3\left(\frac{\mathcal{K}_1}{\mathcal{K}_1-\mathcal{K}_{hb}}\right)ln\left(\frac{\mathcal{K}_1+\mathcal{K}_{hb}}{2\mathcal{K}_{hb}}\right)}{1-N_3+2N_3\left(\frac{\mathcal{K}_{hb}}{\mathcal{K}_1-\mathcal{K}_{hb}}\right)ln\left(\frac{\mathcal{K}_1+\mathcal{K}_{hb}}{2\mathcal{K}_{hb}}\right)}, \tag{17}$$

$$\frac{\mathcal{K}_{hb}}{\mathcal{K}_{nf}}=\frac{1-N_3+2N_3\left(\frac{\mathcal{K}_2}{\mathcal{K}_2-\mathcal{K}_{nf}}\right)ln\left(\frac{\mathcal{K}_2+\mathcal{K}_{nf}}{2\mathcal{K}_{hb}}\right)}{1-N_3+2N_3\left(\frac{\mathcal{K}_{nf}}{\mathcal{K}_2-\mathcal{K}_{nf}}\right)ln\left(\frac{\mathcal{K}_2+\mathcal{K}_{nf}}{2\mathcal{K}_{nf}}\right)}, \tag{18}$$

$$\frac{K_{nf}}{K_f}=\frac{1-N_1+2N_1\left(\frac{\mathcal{K}_3}{\mathcal{K}_3-K_f}\right)ln\left(\frac{K_3+K_f}{2K_f}\right)}{1-N_3+2N_3\left(\frac{\mathcal{K}_f}{K_3-\mathcal{K}_f}\right)ln\left(\frac{\mathcal{K}_3+\mathcal{K}_f}{2\mathcal{K}_f}\right)}. \tag{19}$$

The Yamada Ota model (ternary hybrid) [44] is derived as

$$\frac{\mathcal{K}_{hb}}{\mathcal{K}_{nf}}=\frac{\left(\frac{\mathcal{K}_{hb}}{\mathcal{K}_1}\right)+2N_3^{0.2}\frac{L}{R}-2N_3N_3^{0.2}\frac{L}{R}\left(1-\frac{\mathcal{K}_{hb}}{\mathcal{K}_1}\right)}{\left(\frac{\mathcal{K}_{hb}}{\mathcal{K}_1}\right)+2N_3^{0.2}\frac{L}{R}-N_3\left(1-\frac{\mathcal{K}_{hb}}{\mathcal{K}_1}\right)}, \tag{20}$$

$$\frac{\mathcal{K}_{hb}}{\mathcal{K}_{nf}}=\frac{\left(\frac{\mathcal{K}_{nf}}{\mathcal{K}_2}\right)+2N_2^{0.2}\frac{L}{R}-2N_2N_2^{0.2}\frac{L}{R}\left(1-\frac{\mathcal{K}_{nf}}{\mathcal{K}_2}\right)}{\left(\frac{\mathcal{K}_{nf}}{\mathcal{K}_2}\right)+2N_2^{0.2}\frac{L}{R}-N_3\left(1-\frac{\mathcal{K}_{nf}}{\mathcal{K}_2}\right)}, \tag{21}$$

$$\frac{\mathcal{K}_{nf}}{\mathcal{K}_f}=\frac{\left(\frac{\mathcal{K}_f}{\mathcal{K}_3}\right)+2N_1^{0.2}\frac{L}{R}-2N_1N_1^{0.2}\frac{L}{R}\left(1-\frac{\mathcal{K}_f}{\mathcal{K}_3}\right)}{\left(\frac{\mathcal{K}_f}{\mathcal{K}_3}\right)+2N_1^{0.2}\frac{L}{R}-N_1\left(1-\frac{\mathcal{K}_f}{\mathcal{K}_3}\right)}. \tag{22}$$

The variable density parameter, fluid's absorption number, Prandtl number, Eckert number, Darcy's number, Forchhiermer number, and heat source number are defined as

$$m = \beta^* \Delta t_0, D = a\left(\frac{\left(\nu_f\right)^2}{G\beta^* \Delta t_0}\right), Pr = \frac{\nu_f}{\alpha},$$

$$Ec = \frac{U^2}{\Delta t_0 \left(c_p\right)_f}, \epsilon = \frac{\mu_f}{k}, Fr = \frac{F}{k^{1/2}}, Q^* = \frac{Q}{\left(c_p \rho\right)_f}.$$

Table 2. Thermal properties associated with nanoparticles [44].

Properties	Al_2O_3	CuO	GO	Ethylene glycol
$k[M \cdot m^{-1} \cdot K^{-1}]$	40	20	5000	0.253
$\rho[\, M \cdot L^{-3}]$	3970	6500	2100	1113.5
$C_p[L^2 \cdot T^{-2} \cdot \Theta^{-1}]$	765	540	700	2430

Skin friction coefficient for Newtonian fluid [37] is

$$Cf = \frac{t_w}{\rho_f \left(\nu_f G\beta \Delta T_0\right)^{\frac{2}{3}}}, t_w = \mu_b \left(\nu_f G\beta \Delta T_0\right)^{\frac{1}{3}} \left(\frac{\partial \ddot{U}}{\partial \ddot{Y}}\right)_{\ddot{Y}=0,} \tag{23}$$

$$CfRe = \frac{1}{(1-N_3)^{2.5}(1-N_2)^{2.5}(1-N_1)^{2.5}} \left(\frac{\partial \ddot{U}}{\partial \ddot{Y}}\right)_{\ddot{Y}=0,}, \tag{24}$$

Nusselt number [37] is

$$Nu = \frac{Q_w L}{\Delta T K_f}, Nu = -\frac{\mathcal{K}_f}{\mathcal{K}_{thb}} \left(\frac{\partial T}{\partial \ddot{Y}}\right)_{\ddot{Y}=0,}. \tag{25}$$

3. Numerical solution

The above equations, which are created using primitive variables, can be solved using the Finite Element Method. A detailed description of how to use the finite element method to solve the system of PDEs (partial differential equations) is provided here. First, primitive variables are utilized for easy integration of the problem. Finite element approach is significant rather analytical approach for the case of handing complex problems.

- For complex geometries like porous media, spherical, cylindrical domains, and non-uniform surfaces, the finite element scheme works incredibly well;
- Such nonlinear PDEs are difficult for analytical approaches to solve, but the finite element scheme effectively manages them by discretizing the domain into discrete elements.
- By establishing conditions on the nodes of elements, the finite element scheme enables the flexible implementation of boundary conditions.

Here, primitive variables are defined as

$$\ddot{X} = X, T = \Theta, Y = \ddot{X}^{-\frac{1}{4}} \ddot{Y}, \ddot{V} = \ddot{X}^{-\frac{1}{4}} V, \ddot{U} = \ddot{X}^{\frac{1}{2}} U, \tag{26}$$

Using a primitive variable in Eqs (8)–(10). Now, equations are

$$YXU_X + \frac{1}{2}YU - \frac{Y^2}{4}U_Y + V + YV_Y = 0, \tag{27}$$

$$\begin{aligned}\frac{\nu_f}{\nu_{thb}}\left(X^{-1/2}UU_X + \frac{1}{2}X^{-3/4}UV + X^{-3/4}VU_Y\right) - X^{-1/2}\frac{e^{mT}}{\beta}\frac{\partial}{\partial Y}\left(1 + \frac{1}{\sqrt{\pi_c}}\right)U_Y \\ -X^{-\frac{1}{2}}e^{mT}T - X^{-\frac{1}{2}}\epsilon X^{\frac{1}{2}}U - X^{-\frac{1}{2}}\frac{\nu_f}{\nu_{thb}}FrXU^2 = 0,\end{aligned} \tag{28}$$

$$\begin{aligned}\frac{\mathcal{K}_f}{\mathcal{K}_{thb}}\frac{(\rho c_p)_{thb}}{(\rho c_p)_f}\left(UT_X + X^{-3/4}VT_Y\right) - X^{-1/2}\frac{e^{mT}}{Pr}\left(\frac{1}{Y}\frac{\partial}{\partial Y}(YT_Y)\right) \\ -\left(1 + \frac{1}{\beta}\right)X^{-\frac{1}{2}}\frac{\mathcal{K}_f}{\mathcal{K}_{thb}}\frac{(\rho c_p)_{thb}}{(\rho c_p)_f}\frac{Ec}{2Pr}(U_Y)^2 - X^{-\frac{1}{2}}\frac{\mathcal{K}_f}{Pr\mathcal{K}_{thb}}TQ^* = 0,\end{aligned} \tag{29}$$

Weak Formulations: Integrate over the domain Ω after multiplying each PDE by a test function from the solution space. After multiplying each PDE by a test function from the solution space, integrate over domain Ω.

$$\int_{\eta_E}^{\eta_{E+1}} w_1\left[YXU_X + \frac{1}{2}YU - \frac{Y^2}{4}U_Y + V + YV_Y\right]D\eta = 0, \tag{30}$$

$$\int_{\eta_E}^{\eta_{E+1}} w_2\left[\begin{aligned}\frac{\nu_f}{\nu_{thb}}\left(X^{-\frac{1}{2}}UU_X + \frac{1}{2}X^{-\frac{3}{4}}UV + X^{-\frac{3}{4}}VU_Y\right) - X^{-\frac{1}{2}}\frac{e^{mT}}{\beta}\left(1 + \frac{1}{\beta}\right)\frac{\partial^2\ddot{U}}{\partial\ddot{Y}^2} \\ -X^{-\frac{1}{2}}e^{mT}T - X^{-\frac{1}{2}}\epsilon X^{\frac{1}{2}}U - X^{-\frac{1}{2}}\frac{\nu_f}{\nu_{thb}}FrXU^2\end{aligned}\right]D\eta = 0, \tag{31}$$

$$\int_{\eta_E}^{\eta_{E+1}} w_3\left[\begin{aligned}\frac{\mathcal{K}_f}{\mathcal{K}_{thb}}\frac{(\rho c_p)_{thb}}{(\rho c_p)_f}\left(UT_X + X^{-\frac{3}{4}}VT_Y\right) - X^{-\frac{1}{2}}\frac{e^{mT}}{Pr}\left(\frac{1}{Y}\frac{\partial}{\partial Y}(YT_Y)\right) \\ -\left(1 + \frac{1}{\beta}\right)X^{-\frac{1}{2}}\frac{\mathcal{K}_f}{\mathcal{K}_{thb}}\frac{(\rho c_p)_{thb}}{(\rho c_p)_f}\frac{Ec}{2Pr}(U_Y)^2 - X^{-\frac{1}{2}}\frac{\mathcal{K}_f}{Pr\mathcal{K}_{thb}}TQ^*\end{aligned}\right]D\eta = 0. \tag{32}$$

Discretization of domain: Segment the domain Ω into finite components, such as triangle elements.

$$U^n = \sum_{i=1}^{n} N_i\widehat{U}_i\,, T^n = \sum_{i=1}^{n} N_iT_i\,, V^n = \sum_{i=1}^{n} N_i\widehat{V}_i, \tag{33}$$

Calculations of Stiffness elements: The calculations of stiffness elements are mentioned here

$$K_A^{ij} = \int_\Omega \left[YXN_i \frac{\partial N_j}{\partial X} + \frac{1}{2} YN_iN_j - \frac{Y^2}{4} \frac{\partial N_i}{\partial Y} + N_iN_j + YN_i \frac{\partial N_j}{\partial Y} \right] D\Omega, \tag{34}$$

$$K_B^{ij} = w_U \frac{\nu_f}{\nu_{thb}} \int_\Omega \left[\left(X^{-\frac{1}{2}} N_i U \frac{\partial N_j}{\partial X} + \frac{1}{2} X^{-\frac{3}{4}} N_i UV + X^{-\frac{3}{4}} N_i V \frac{\partial N_j}{\partial Y} \right) \right] D\Omega, \tag{35}$$

$$\begin{aligned} &- \int_\Omega w_U X^{-\frac{1}{2}} e^{mT} / \beta \frac{\partial}{\partial Y} \left(1 + \frac{1}{\sqrt{\pi_c}} \right) \frac{\partial N_j}{\partial Y} D\Omega - w_U \int_\Omega X^{-\frac{1}{2}} e^{mT} T N_i \, D\Omega \\ &\quad - w_U \int_\Omega X^{-\frac{1}{2}} \frac{\nu_f}{\nu_{thb}} FrXU^2 N_j D\Omega, \end{aligned} \tag{36}$$

$$\begin{aligned} &w_T \int_\Omega \frac{\mathcal{K}_f}{\mathcal{K}_{thb}} \frac{(\rho c_p)_{thb}}{(\rho c_p)_f} \left(N_i U \frac{\partial N_i}{\partial X} + X^{-3/4} N_i V \frac{\partial N_j}{\partial X} \right) D\Omega - \int_\Omega w_T X^{-\frac{1}{2}} \frac{e^{mT}}{Pr} \left(\frac{1}{Y} \frac{\partial}{\partial Y} \left(Y \frac{\partial N_j}{\partial Y} \right) \right) D\Omega \\ &- w_T \int X^{-\frac{1}{2}} \frac{\mathcal{K}_f}{\mathcal{K}_{thb}} \frac{(\rho c_p)_{thb}}{(\rho c_p)_f} \frac{Ec}{2Pr} \left(\frac{\partial U}{\partial Y} \right)^2 N_j D\Omega - w_T \int_\Omega X^{-\frac{1}{2}} \frac{\mathcal{K}_f}{Pr \mathcal{K}_{thb}} Q^* N_j D\Omega. \end{aligned} \tag{37}$$

The Global stiffness matrix is derived as

$$[K] = \begin{bmatrix} K_A & 0 & 0 \\ 0 & K_M & 0 \\ 0 & 0 & K_E \end{bmatrix}, \tag{38}$$

Assembly Process: Use the weak form of the basic functions to calculate the element stiffness matrix and element load vector for each element. The global matrix is

$$[K]\{U, V, \Theta\} = \{F\}. \tag{39}$$

Solve the system of equations: Use the proper numerical techniques to solve the linear or nonlinear algebraic system, such as the Gaussian elimination approach. Verifying that the maximum relative change between two successive iteration levels falls below 10 at each stage is known as the convergence of the solution. The flow chart of the numerical approach is mentioned in Figure 3. Table 3 describes the comparative results of heat transfer distribution with a published study [37] when $Q^* = 0, Fr = \epsilon = 0, Ec = 0, N_3 = N_1 = 0$, and $N_2 = 0$.

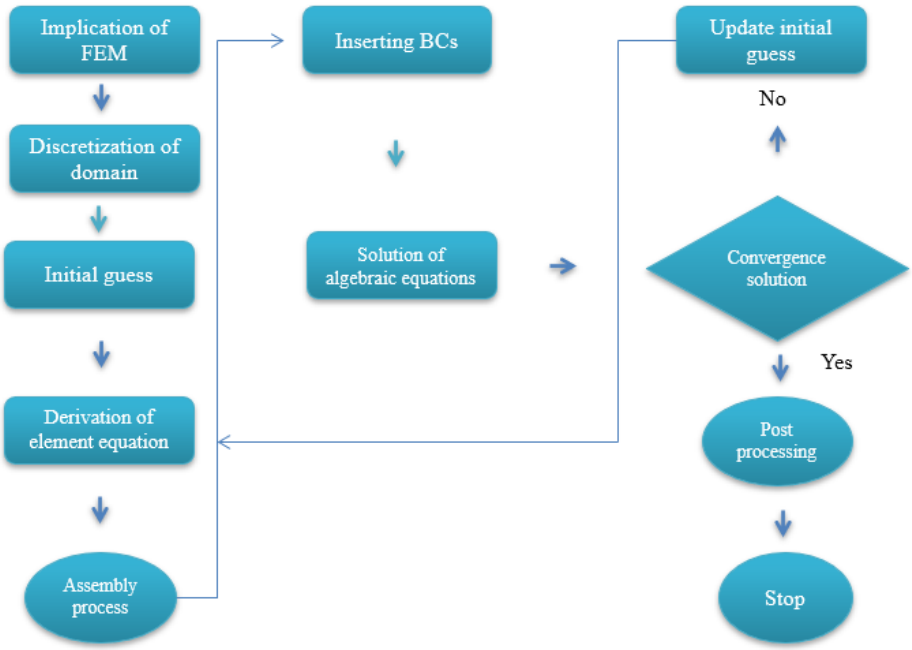

Figure 3. Flow diagram of the finite element approach.

Error analysis: It is noticed that error analysis is derived as

$$ER = \left|\omega^{j} - \omega^{j-1}\right|, \tag{40}$$

and convergence condition is

$$Max\left|\omega^{j} - \omega^{j-1}\right| < 10^{-8}. \tag{41}$$

Table 3. Validation of numerical results with the published investigation [37] when $Q^{*} = 0, Fr = \epsilon = 0, Ec = 0, N_3 = N_1 = 0$ and $N_2 = 0$.

	Published work (finite difference method) [37]	Current model (finite element method)
Pr	Temperature distribution	Temperature distribution
6.7	0.0011	0.0016832403
10.0	0.0009	0.0006710710
20.0	0.0005	0.0007924171

4. Results and discussion

The two-dimensional motion of steady Casson fluid is considered on a jet. The suspension of ternary hybrid nano-fluid is assumed. Darcy's Forchhiermer law and heat sink are considered. ANOVA of Box–Behnken Design is estimated for Nusselt number and divergent velocity. The chosen parameter ranges guarantee accurate modeling of fluid flow and heat transfer. The ranges of dimensionless parameters are $0.0 \leq D \leq 4.0, 0.0 \leq Ec \leq 5.0, -5.0 \leq Q^{*} \leq 4.5, 0.0 \leq D \leq 7.0, 0.0 \leq m \geq 2.5, 0.0 \leq Fr \leq 3, 0.0 \leq \epsilon \geq 7.0, 0.0 \leq N_3 \leq 0.006, 0.0 \leq N_1 \leq 0.007, 0.0 \leq N_2 \leq 0.005, 0.0 \leq \beta \leq 3.0, 5 \leq Pr \geq 12$.The detailed explanations are mentioned below.

In Figures 4–7, green lines are associated with THBN, HN is described by hybrid nanofluid, and

NF describes the role of blue lines. Figure 4 estimates the variation of Fr on U in the presence of tri-hybrid nano-particles. With an increment of Fr, the velocity field declines. Darcy-Forchheimer law combines inertial and viscous effects to describe fluid flow through porous media. The Forchheimer term is added to Darcy's law, which applies to slow, viscous flow to account for higher flow velocities where inertial effects become noticeable. In porous media, inertial resistance is produced due to the Forchheimer parameter. It causes a rise in the nonlinear drag force, which declines fluid motion and lowers velocity, which lowers the flow rate. THBN on motion is higher than NF and HB on motion. The variation of m on the velocity field is captured in Figure 5. The curves of U are inclined when m is enhanced. Here, m is called the power law number. In such models, the power-law number m can describe how the resistance to flow varies with velocity or shear rate. Fluid density variations are amplified by increasing the variable density parameter, which raises inertia and motion resistance. This causes the velocity field to decrease and the flow to slow down due to a higher momentum diffusion rate. Figure 7 captures the behavior of D on velocity curves. The velocity field increases when D is enhanced. Here, D is known as the fluid's absorption number. It is a dimensionless figure that expresses the quickly a fluid (or energy) is absorbed into a medium about other transport effects. The role of Ec on the temperature profile is visualized in Figure 8 considering THBNF, HNF, and nanofluid. The concept of viscous dissipation is utilized for modeling of Eckert number. When the Eckert number is enhanced, more heat energy is dissipated. The temperature profile is enhanced. The amount of heat energy for nanofluid is less than the heat energy for THBNF and HNF. Figure 9 exhibits the trend of the heat sink on heat including THNF, HNF and nanofluid. The heat sink is denoted by Q^* which is proportional to temperature difference. An increment of heat sink deals with an enhancement of heat energy. The heat source parameter (Q^*) controls both heat absorption (negative Q^*) and heat generation (positive Q^*). It has a major effect on heat transfer in a number of applications, such as industrial heat exchangers, electronic cooling, and nuclear reactors. The change of D on heat energy is estimated in Figure 10 considering nanofluid, HNF and THNF. Thermal energy is boosted when D is enhanced. Here, D is called the fluid's absorption number. The production of heat energy for nanofluid is less than heat energy for HNF, and THNF. The variation of m on the velocity curve is captured in Figure 11 including THNF, NF, and hybrid nanofluid. The velocity curve is enhanced with the change of m. Convective heat transfer efficiency is decreased when fluid density variations are enhanced by an increase in the variable density parameter. As a result, the fluid retains more heat, raising the temperature field and thermal energy distribution. The variation of Fr and ϵ on divergent velocity is estimated in Figure 12 considering THNF, HNF, and nanofluid. Divergent velocity increases when Fr and ϵ are increased. Resistance to fluid expansion is decreased by increasing inertial and nonlinear effects while increasing Fr and ϵ. This encourages flow divergence, which raises divergent velocity because of stronger inertial forces. The variation of D and m on Cf is tackled in Figure 13. The skin friction coefficient is declined when D and m are increased. While increasing m amplifies density variations and encourages flow expansion, increasing D improves fluid absorption and lowers local resistance. Therefore, divergent velocity decreases. The production of tri-hybrid nanofluid is greater than the production of HNF and nanofluid. Figure 14 shows the roles of m and Q^* on the Nusselt number. It is observed that the Nusselt number enhances when m and Q^* are increased. The variation of D and M on the Nusselt number is observed in Figure 15 for the case of hybrid nanofluid and tri-hybrid nano-fluid. The heat transfer is improved when the buoyancy-driven convection is enhanced when m is enhanced. An increasing in Q^* supplies more heat energy, which enhances the temperature gradients. Therefore, Nusselt number increases. Figure 16 describes the change of m and Q^* on the

Nusselt number for the Xue and Yamada Ota ternary hybrid nanofluid model. It is noticed that the heat transfer rate for Yamada Ota ternary hybrid nanofluid is higher than Xue-ternary hybrid nanofluid. It is used because of their precision in predicting thermal conductivity and effective viscosity in intricate multiphase flows, the Xue and Yamada-Ota hybrid nanofluid models were chosen. Yamada-Ota's model is perfect for high-performance cooling applications because it more accurately depicts the interactions between nanoparticles, which results in higher heat transfer rates. Despite its conservatism, Xue's model is still applicable to stability analysis. Their comparison ensures better thermal management by offering insights into how to optimize hybrid nanofluids for energy and industrial applications. The production of TNF is greater than HNF. Table 4 describes the variation of Ec, m and D on Nusselt number for HNF and THNF. The production of heat transfer rate for THNF is less than HNF. Nusselt number declines when Ec is enhanced. The rate of heat transfer decreases when m is enhanced. Heat transfer rate decreases with the change of D. The production of Nusselt number THNF is greater than HNF and nanofluid.

Box–Behnken design method: Nusselt number and divergent velocity are determined with the approach of the Box–Behnken design method. The Box–Behnken design method (see Figure 17) is a statistical technique for response variable optimization that is used to analyze the Nusselt number and divergent velocity. This approach systematically assesses the effects of several variables and how they interact. It effectively ascertains the ideal parameters for improved fluid system flow and heat transfer. The parameters and factor levels that are utilized in the Box–Behnken Design (BBD) for the analysis of skin friction coefficients (SKF) are listed in Table 5. The variables are the magnetic parameter (B, C) between 0.3 and 0.9, the power-law index (m, B) between 1 and 6, and the Forchheimer number (Fr, A) between 0.1 and 0.8. These ranges enable a thorough assessment of how they affect the responses. The parameters and factor ranges utilized in the Box–Behnken Design (BBD) for Nusselt number analysis are shown in Table 6. The variables include the diffusion parameter (D, C) between 0.1 and 0.8, the heat source parameter (Q*, B) between 2 and 8, and the Eckert number (Ec, A) between 0.3 and 0.9. These ranges aid in the investigation of their impact on heat transfer. BBD matrix for calculating the skin friction coefficient (cf) with factors Fr, m, and B at different levels is displayed in Table 7. The 15 runs in the table each have unique parameter combinations and matching Cf responses. The ANOVA results for the skin friction coefficient (Cf) are displayed in Table 8, highlighting the importance of the model terms. The linear term m (30.70%) and interaction effects like $Fr{\times}m$ (22.17%) are the major contributors to the model's 94.98% explanation of the variation, whereas the error only makes up 2.70 percent. BBD matrix for calculating the Nusselt number (Nu) with factors Ec, Q^*, and D at different levels is shown in Table 9. It includes 15 runs that demonstrate particular parameter combinations and the Nu responses that correspond to them to evaluate the behavior of heat transfer. The Nusselt number (Nu) analysis is summarized in the ANOVA table, which also displays the significance of the model with an F-value of 3.22 and a P-value of 0.021. Quadratic terms (Ec: P = 0.029) and interactions such as Ec∗D (P=0.002) make significant contributions, demonstrating their influence on heat transfer. According to the ANOVA table 10, linear, square, and interaction terms all contribute to the model's significance (P = 0.021). Low P-values for important parameters like $Q*$, D, and their interactions show how strongly they affect the Nusselt number. Figure 19 depicts the residuals roughly following a straight line, which indicates normality, according to the Normal Probability Plot. Despite the residuals clustering for small fitted values, the Versus Fits plot shows no discernible pattern, indicating homoscedasticity. The model's assumptions are supported by the Histogram and Versus Order plots, which display a random residual distribution devoid of trends.

The normality of the residuals is roughly indicated by the normality plot, with minor deviations at the extremes (see Figure 18). There are no discernible patterns in the Versus Fits and Versus Order plots, indicating constant variance and independence. The residuals' normal distribution is validated by the histogram, which supports symmetry. Figures 20a,b,c describe the role of contour plots of Fr, M, B on the Skin friction coefficient. Figures 21a,b,c describe contour plots of Ec, Q^*, D on the Skin friction coefficient. The change of Q^* and Ec on the Nusselt number is visualized in Figure 13. The Nusselt number is a decline function with the change of Q^* and Ec.

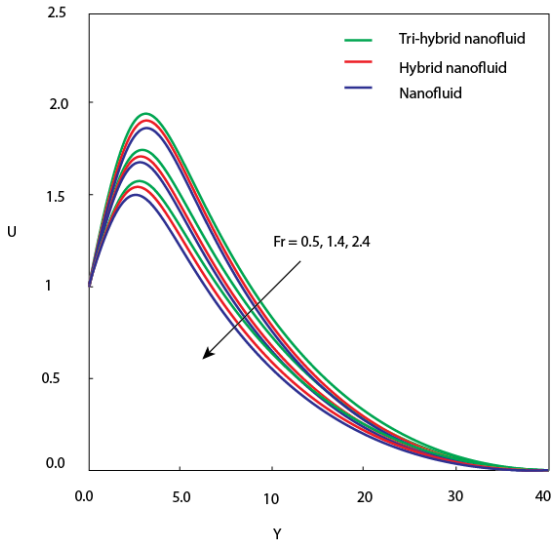

Figure 4. Variation of Fr on U.

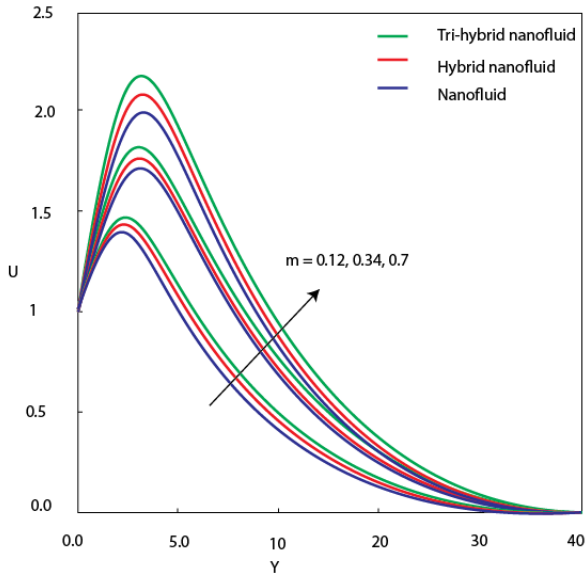

Figure 5. Variation of m on U.

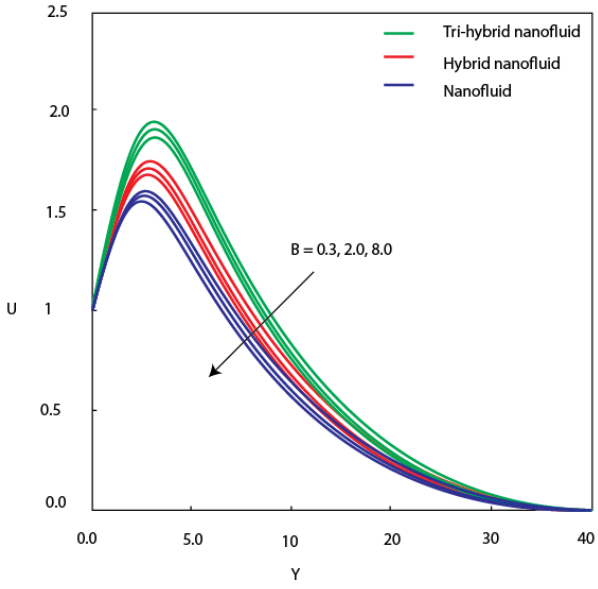

Figure 6. Variation of B on U.

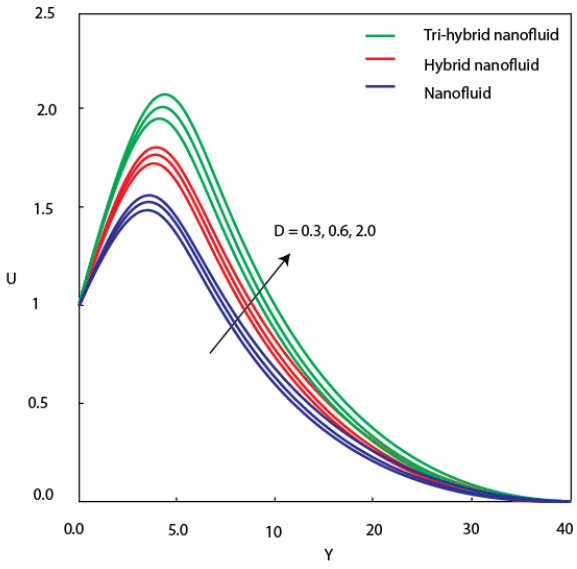

Figure 7. Variation of D on U.

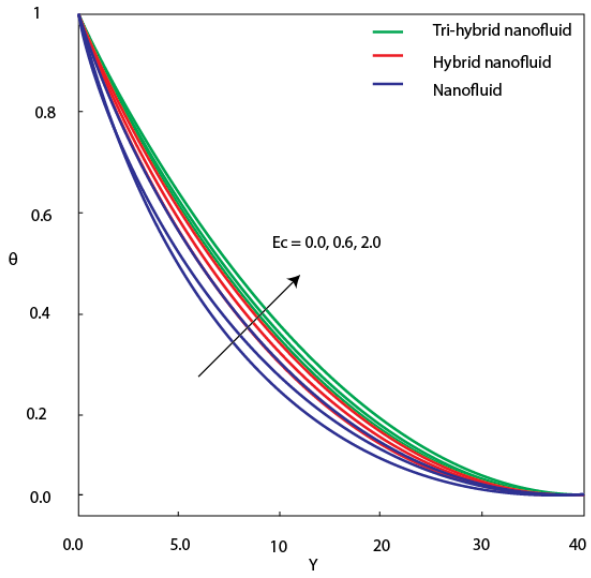

Figure 8. Variation of Ec on θ.

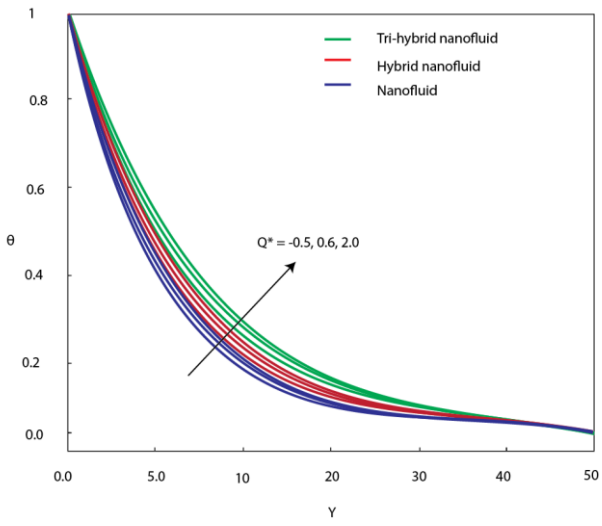

Figure 9. Variation of Q^* on θ.

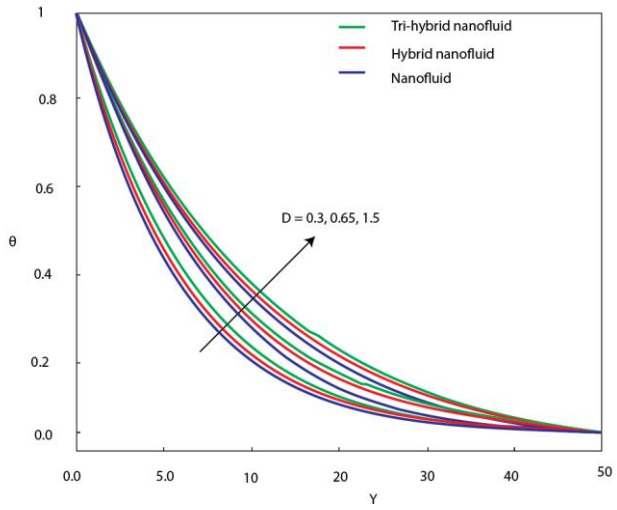

Figure 10. Variation of D on θ.

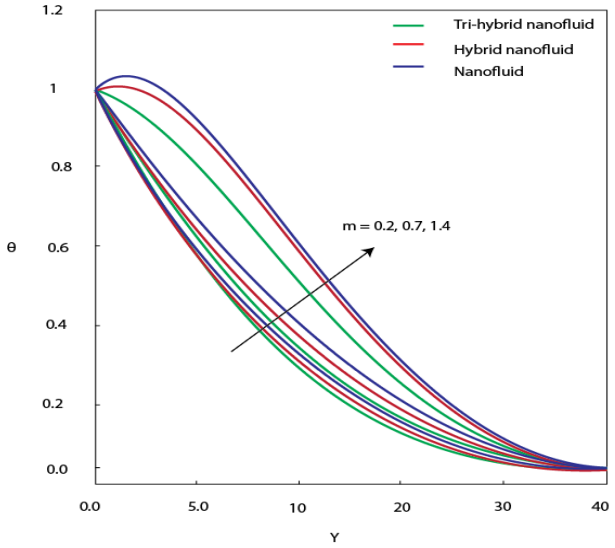

Figure 11. Variation of m on θ.

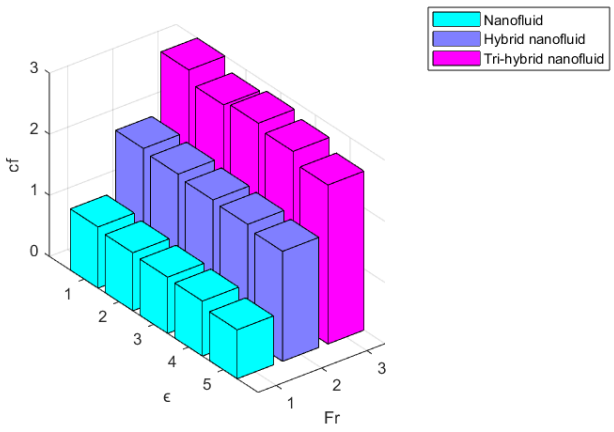

Figure 12. Variation of Fr and ϵ on Cf.

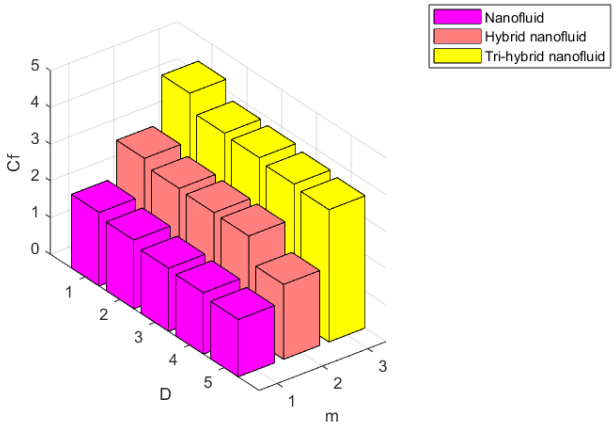

Figure 13. Variation of D and m on Cf.

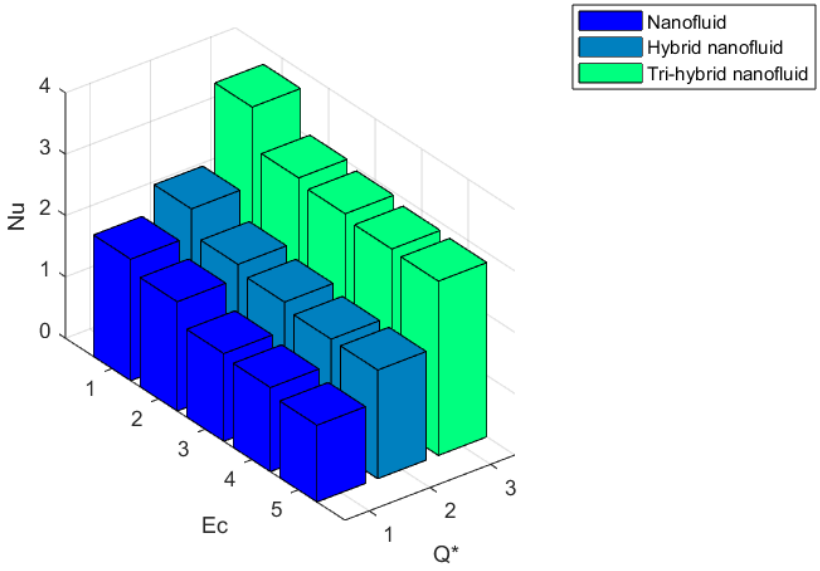

Figure 14. Variation of $Q*$ and Ec on Nu.

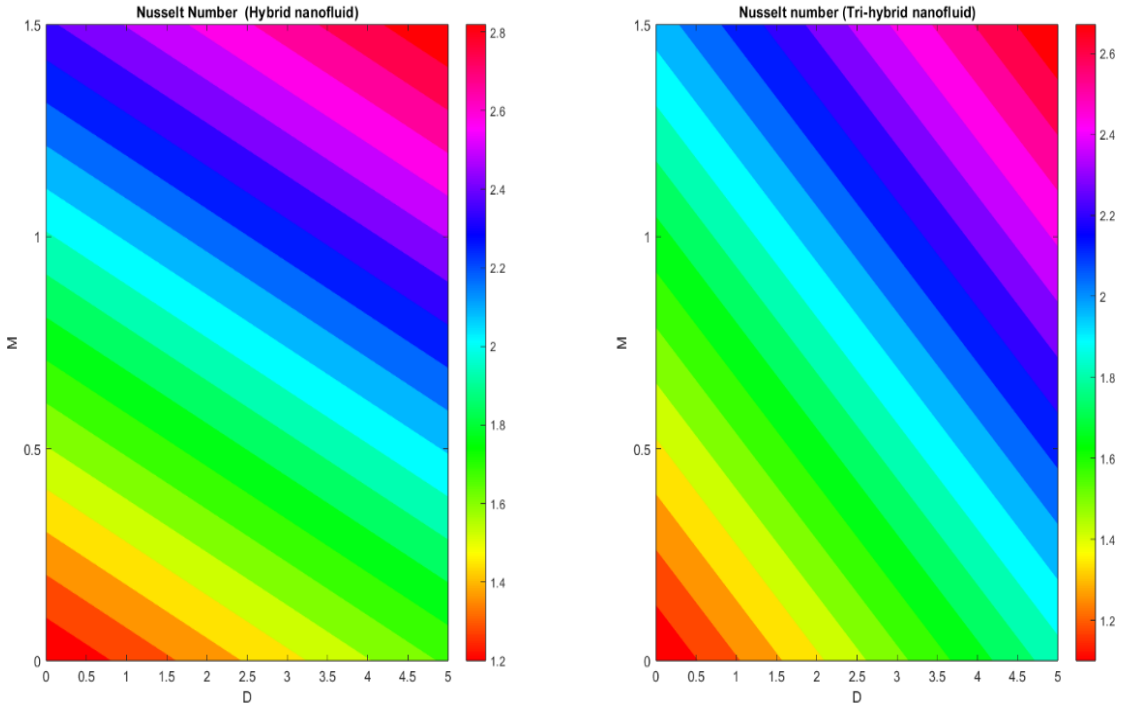

Figure 15. Variation of D and M on Nusselt number.

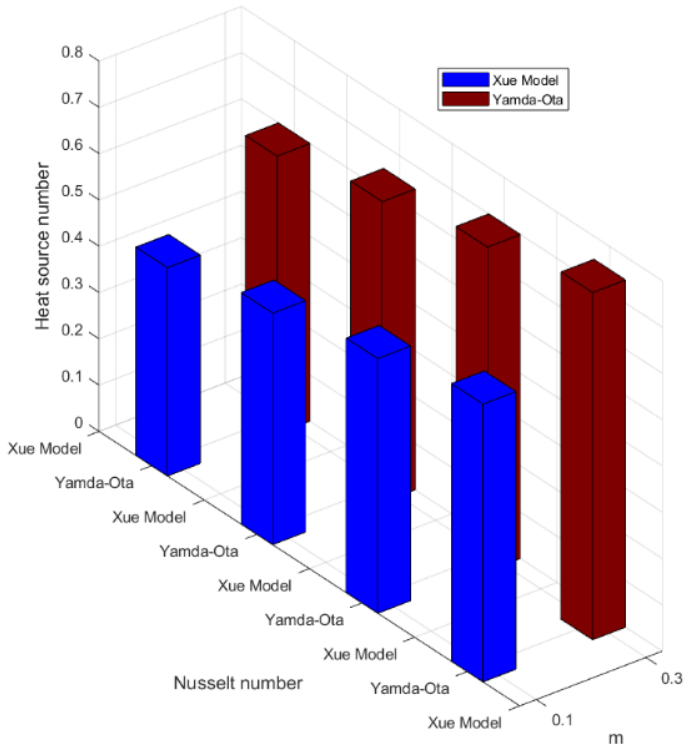

Figure 16. Variation of m and Q^* on Nusselt number.

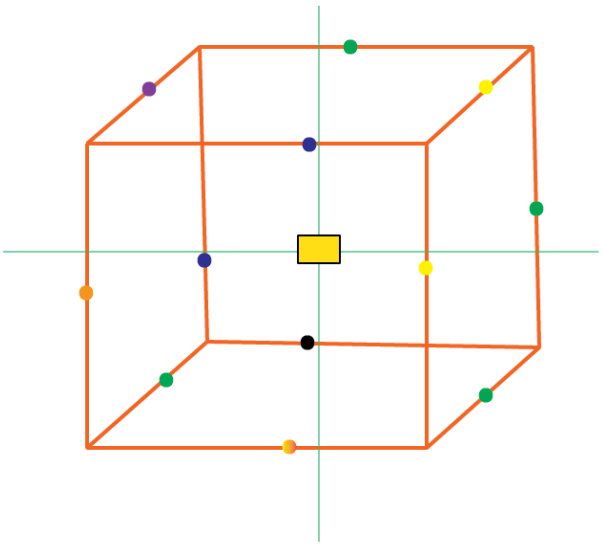

Figure 17. Design of Box–Behnken.

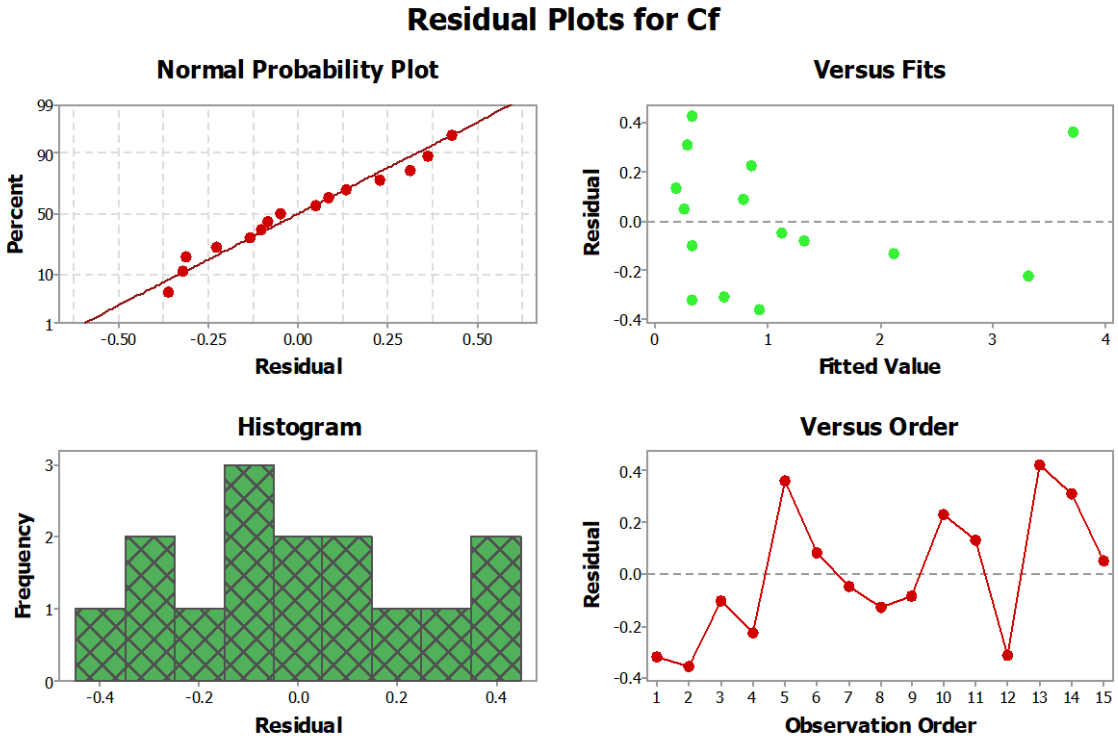

Figure 18. Residual plots of Cf.

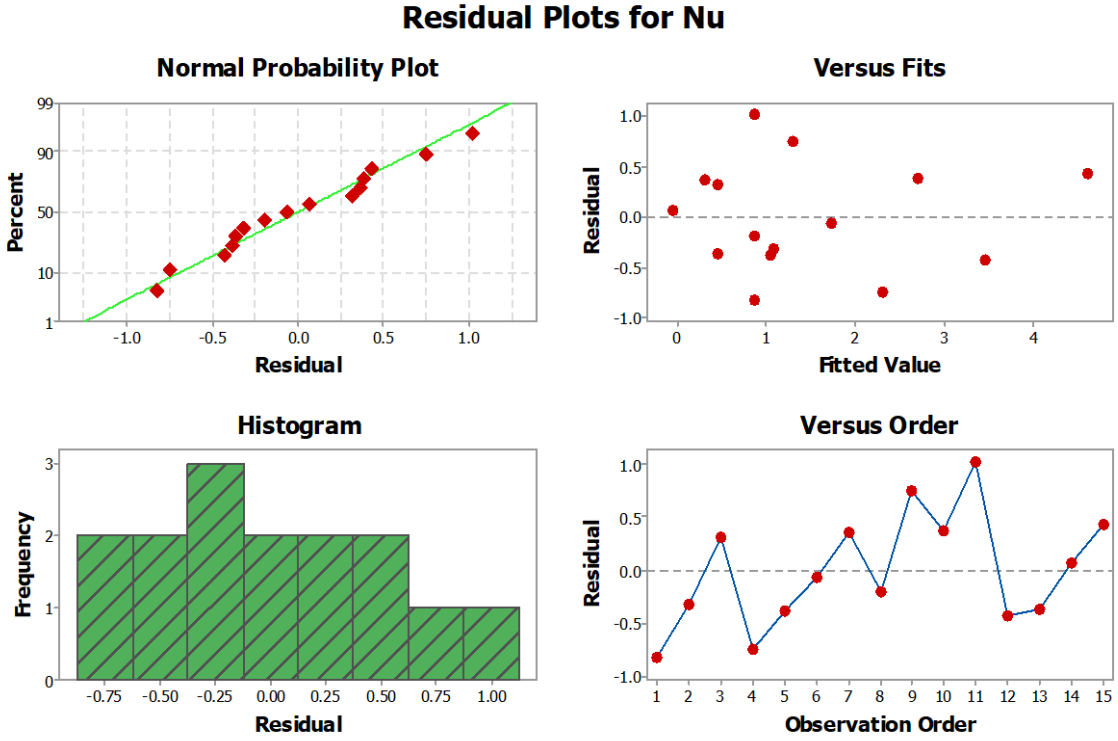

Figure 19. Residual plots of Nusselt number.

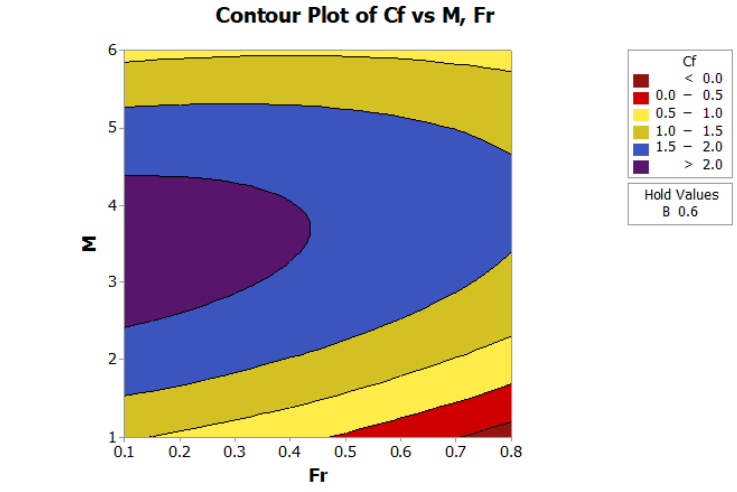

(a)

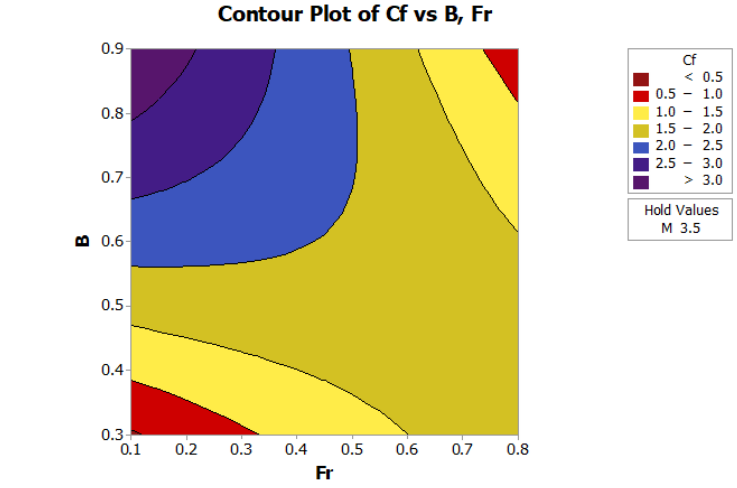

(b)

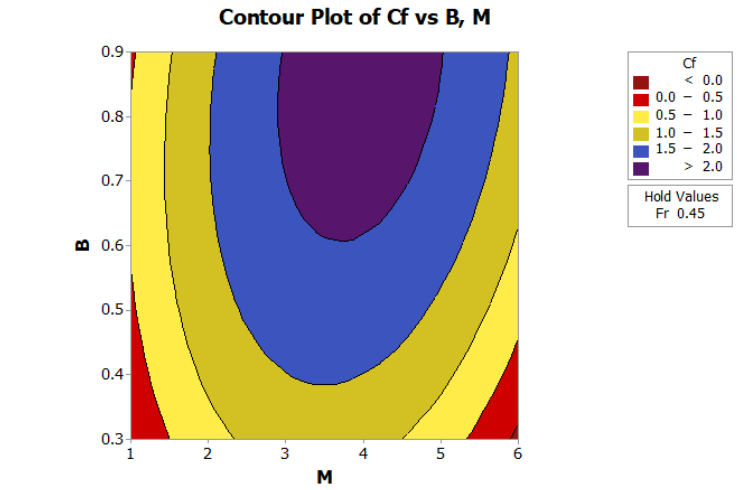

(c)

Figure 20. Contour plots of Fr, M, B on Skin friction coefficient.

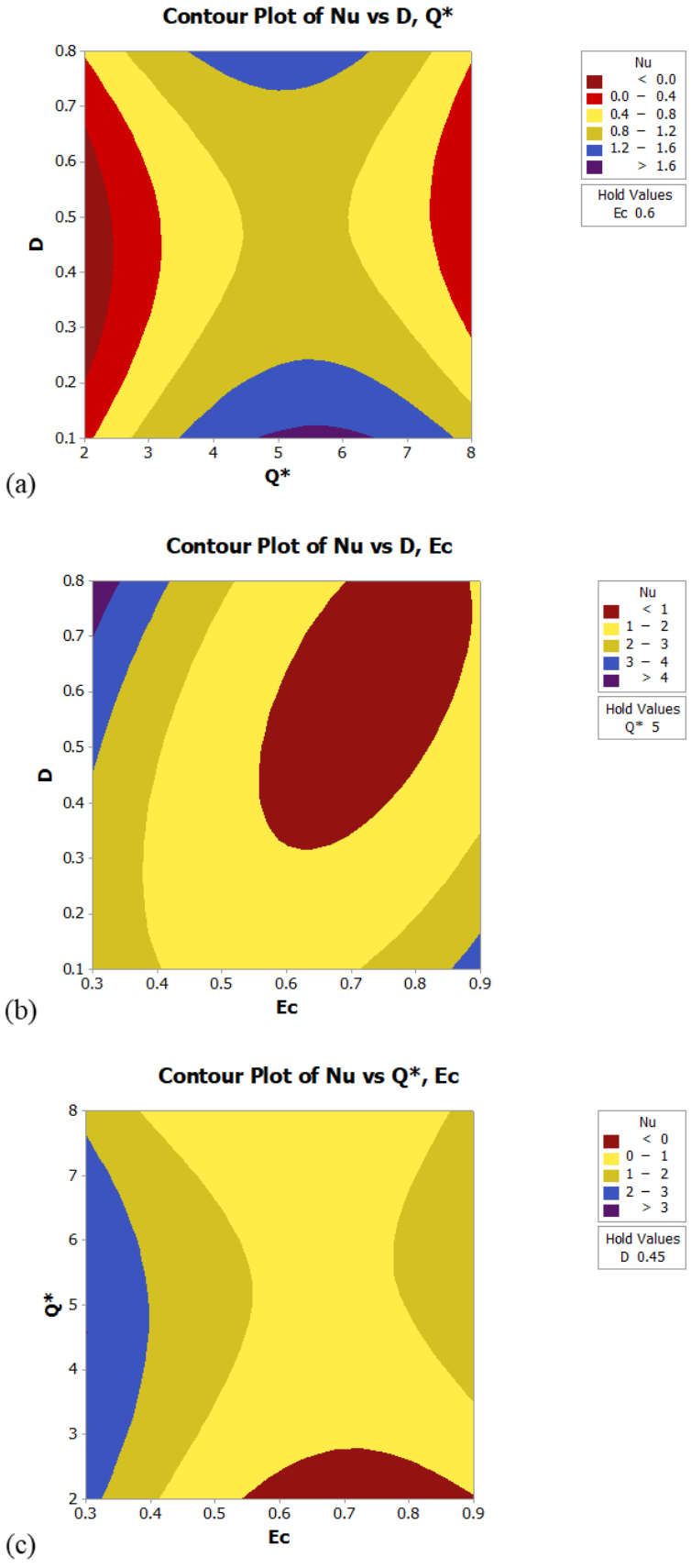

Figure 21. Contour plots of Ec, Q^*, D on the Skin friction coefficient.

Table 4. Variation of different parameters on Nusselt number for hybrid and tri-hybrid nanofluid.

		Hybrid nanofluid	Tri-hybrid nanofluid
		Nusselt number	Nusselt number
	0.0	0.08332359237	1.05507030932
Ec	0.5	0.06487278066	1.04598329240
	2.0	0.05633812980	1.12117538253
	0.0	0.04820572018	1.09413641865
m	0.5	0.03043927133	1.07157245228
	2.0	0.02588185778	1.05243604710
	0.0	0.01903887454	1.04345326085
D	0.5	0.01245668658	1.02648986627
	2.0	0.006116108897	1.00315562782

Table 5. Responses and parameters utilized in the BBD associated with SKF.

Parameters	Factors	Low	High
Fr	A	0.1	0.8
m	B	1	6
B	C	0.3	0.9

Table 6. Responses and parameters utilized in the BBD associated with Nusselt number.

Parameters	Factors	Low	High
Ec	A	0.3	0.9
$Q*$	B	2	8
D	C	0.1	0.8

Table 7. Matrix of BBD for Cf.

Run	A	B	C	Fr	m	B	Cf
1	0	0	0	0.45	3.5	0.6	0.01
2	-1	-1	0	0.1	1	0.6	0.56
3	0	0	0	0.45	3.5	0.6	0.23
4	0	1	1	0.45	6	0.9	3.09
5	1	1	0	0.8	6	0.6	4.08
6	1	-1	0	0.8	1	0.6	0.871
7	0	0	1	0.45	6	0.3	1.075
8	1	1	0	0.8	3.5	0.9	1.982
9	-1	-1	-1	0.1	6	0.6	1.245
10	0	0	-1	0.45	1	0.3	1.076
11	-1	0	-1	0.1	3.5	0.3	0.32
12	1	0	-1	0.8	3.5	0.3	0.3
13	0	0	0	0.45	3.5	0.6	0.76
14	-1	0	1	0.1	3.5	0.9	0.6
15	1	-1	1	0.45	1	0.9	0.3

Table 8. ANOVA study for Cf.

Source	DF	Adj SS	Adj MS	F-Value	P-Value	Contributions
Model	9	17.2706	1.91896	10.51	0.009	94.98%
Linear	3	9.4039	3.13462	17.17	0.005	51.72%
Fr	1	2.5403	2.54026	13.91	0.014	13.97%
m	1	5.5828	5.58281	30.57	0.003	30.70%
B	1	1.2808	1.28080	7.01	0.046	7.04%
Square	3	3.8353	1.27843	7.00	0.031	21.09%
m*m	1	3.4756	3.47558	19.03	0.007	1.98%
B*B	1	0.0247	0.02465	0.13	0.728	18.98%
2-Way Interaction	3	4.0315	1.34382	7.36	0.028	0.14%
Fr*m	1	1.5926	1.59264	8.72	0.032	22.17%
m*B	1	1.9474	1.94742	10.66	0.022	8.76%
Error	5	0.9131	0.18261		0.003	2.70%
Lack-of-Fit	3	0.6158	0.20527	1.38	0.446	10.71%
Pure Error	2	0.2973	0.14863			5.02%
Total	14	18.1837				100%

Table 9. Matrix of BBD for Nu.

Run	A	B	C	Ec	Q^*	D	Nu
1	0	0	0	0.6	5	0.45	0.0430
2	0	1	-1	0.6	8	0.10	0.7600
3	0	-1	1	0.6	2	0.80	0.7630
4	-1	-1	0	0.3	2	0.45	1.5620
5	1	0	1	0.9	5	0.80	0.6720
6	-1	1	0	0.3	8	0.45	1.6720
7	0	-1	1	0.6	2	0.10	0.6720
8	0	0	0	0.6	5	0.45	0.6734
9	1	1	0	0.9	8	0.45	2.0400
10	-1	0	-1	0.3	5	0.10	3.0820
11	0	0	0	0.6	5	0.45	1.8930
12	1	0	-1	0.9	5	0.10	3.0230
13	0	1	1	0.6	8	0.80	0.0894
14	1	-1	0	0.9	2	0.45	0.0054
15	-1	0	1	0.3	5	0.80	5.0530

Table 10. ANOVA study for Nu.

Source	DF	Adj SS	Adj MS	F-Value	P-Value
Model	9	23.3735	2.5971	3.22	0.021
Linear	3	4.3791	1.4597	1.81	0.034
Ec	1	3.9601	3.9601	4.92	0.077
Q*	1	0.3038	0.3038	0.38	0.003
D	1	0.1151	0.1151	0.14	0.002
Square	3	13.2535	4.4178	5.48	0.049
Ec*Ec	1	7.4266	7.4266	9.22	0.029
Q**Q*	1	3.461	3.461	4.3	0.093
2-Way Interaction	3	5.741	1.9137	2.38	0.032
Ec*Q*	1	0.926	0.926	1.15	0.333
Ec*D	1	4.6699	4.6699	5.8	0.002
Q**D	1	0.145	0.145	0.18	0.0042
Error	5	4.0273	0.8055		0.0012
Lack-of-Fit	3	2.2582	0.7527	0.85	0.025
Pure Error	2	1.7691	0.8846		0.021
Total	14	27.4008			

The Regression equation of Nusselt number and divergent velocity is defined as

$$Cf = 4.50 - 5.75Fr - 1.635m - 4.51B - 3.15Fr^2 + 0.1552m^2 + 0.91B^2 + 0.721Frm + 3.34FrB + 0.930mB. \tag{42}$$

$$Nu = 4.61 - 19.30Ec + 0.902Q^* + 1.82D + 15.76Ec^2 - 0.1076Q^{*2} + 5.47D^2 + 0.535EcQ - 10.29EcD - 0.181Q^*D. \tag{43}$$

The limitations of BBD are listed below.

- According to BBD, the output responses and input parameters have a quadratic relationship. For highly non-linear problems, BBD might not be able to capture intricate relationships.
- BBD needs many simulations as the number of input factors rises;

The computational cost rises dramatically for problems with multiple parameters.

5. Conclusions

Two-dimensional Casson rheology with Darcy's Forchhiermer law is utilized in Jet. The correlation of THNF is utilized with heat sink and viscous dissipation. The finite difference approach is used for numerical outcomes. The key points are listed below.

- The motion of nanofluid is enhanced when Forchiermer number and B are enhanced. However, the motion of the nanofluid is decreased when m and D are enhanced;
- The motion of THNF is greater than the motion of HNF and nanofluid;
- Thickness related to TBLT for THNF is less than the thickness of TBLT of HNF and nanofluid;
- The temperature profile is boosted when heat sink and Eckert number, D, and the power law index number are enhanced;

- THNF has remarkable achievement in heat transfer rate on the divergent velocity rather than HNF on the divergent velocity;
- According to the ANOVA, the model's reliability is confirmed by the 94.98% contribution, which is significant and dominated by linear terms (51.72%), especially mmm (30.70%), and significant two-way interactions. Error contributes only 2.70%.
- The choice of Go, CuO , and Al_2O_3 with Casson fluid and ethylene glycol is founded on stability and thermal and rheological properties. Such a choice is made to determine the heat transfer and fluid stability for engineering and industrial applications. Further, the combination of three nanofluids in a base fluid is better than a single nanofluid.

Limitations

- The mesh density and quality have an impact on the accuracy of the finite element method. Slow convergence, errors, and instabilities can result from a bad mesh.
- Research has indicated that the Yamada–Ota model may overestimate in some situations because it frequently predicts higher temperatures than the Xue model.
- When dealing with three or four independent variables, the Box-Behnken method works well; however, as the number of input parameters increases, it becomes computationally costly and ineffective.
- When turbulence occurs in high-velocity or highly inertial flows, the Darcy-Forchheimer model may not hold because it assumes a particular type of resistance in porous media.

Future directions: The current model is based on Casson fluid in a Vertical jet using a ternary hybrid nanofluid with BBD. It is mentioned that this model can be solved in different non-Newtonian fluids like Jeffery fluid, Maxwell fluid, hyperbolic tangent fluid, Second-grade fluid, micropolar fluid, and Williamson fluid. In the future, the correlations of tetra hybrid nanofluid will be used for the measurement of thermal energy. Also, non-Fourier's law will be implemented. Such models can be used in biomedical engineering, power generation, automotive, and thermal management process.

Author contributions

Umar Nazir: Conceptualization, Methodology, Software, Formal analysis, Writing—original draft preparation, Project administration; Abdelaziz Nasr: Conceptualization, Methodology, Software, Validation, Formal analysis, Investigation, Resources, Writing—review and editing, Supervision, Funding acquisition. All authors have read and agreed to the published version of the manuscript.

Use of Generative-AI tools declaration

The authors declare they have not used Artificial Intelligence (AI) tools in the creation of this article.

Funding

This research work was funded by Umm Al-Qura University, Saudi Arabia under grant number 25UQU4340531GSSR01.

Acknowledgments

The authors extend their appreciation to Umm Al-Qura University, Saudi Arabia for funding this research work through grant number 25UQU4340531GSSR01.

Conflicts of Interest

The authors declare no conflicts of interest.

References

1. M. Sohail, U. Nazir, A. Singh, A. Tulu, M. J. Khan, Finite element analysis of cross fluid model over a vertical disk suspended to a tetra hybrid nanoparticles mixture, *Sci. Rep.*, **14** (2024), 1520. https://doi.org/10.1038/s41598-024-51262-w
2. M. D. Shamshuddin, N. Akkurt, A. Saeed, P. Kumam, Radiation mechanism on dissipative ternary hybrid nanoliquid flow through rotating disk encountered by Hall currents: HAM solution, *Alex. Eng. J.*, **65** (2023), 543–559.https://doi.org/10.1016/j.aej.2022.10.021
3. M. D. Shamshuddin, Z. Raizah, N. Akkurt, V. S. Patil, S. M. Eldin, Case study of thermal and solutal aspects on non-Newtonian Prandtl hybrid nanofluid flowing via stretchable sheet: Multiple slip solution, *Case Stud. Therm. Eng.*, **49** (2023), 103186. https://doi.org/10.1016/j.csite.2023.103186
4. M. D. Shamshuddin, S. O. Salawu, S. Panda, S. R. Mishra, A. Alanazy, M. R. Eid, Thermal case exploration of electromagnetic radiative tri-hybrid nanofluid flow in Bi-directional stretching device in absorbent medium: SQLM analysis, *Case Stud. Therm. Eng.*, **60** (2024), 104734. https://doi.org/10.1016/j.csite.2024.104734
5. A. Ali, Z. Khan, M. Sun, T. Muhammad, K. A. M. Alharbi, Numerical investigation of heat and mass transfer in micropolar nanofluid flows over an inclined surface with stochastic numerical approach, *Eur. Phys. J. Plus*, **139** (2024), 957. https://doi.org/10.1140/epjp/s13360-024-05676-0
6. Z. Khan, W. F. Alfwzan, A. Ali, N. Innab, S. Zuhra, S. Islam, Intelligent computing for electromagnetohydrodynamic bioconvection flow of micropolar nanofluid with thermal radiation and stratification: Levenberg–Marquardt backpropagation algorithm, *AIP Adv.*, **14** (2024), 035101. https://doi.org/10.1063/5.0187124
7. A. M. Alqahtani, M. Bilal, F. A. A. Elsebaee, S. M. Eldin, T. R. Alsenani, A. Ali, Energy transmission through carreau yasuda fluid influenced by ethylene glycol with activation energy and ternary hybrid nanocomposites by using a mathematical model, *Heliyon*, **9** (2023), e15074. ttps://doi.org/10.1016/j.heliyon.2023.e14740
8. K. U. Rahman, Z. Mahmood, S. U. Khan, A. Ali, Z. Li, I. Tlili, Enhanced thermal study in hybrid nanofluid flow in a channel motivated by graphene/Fe_3O_4 and Newtonian heating, *Results Eng.*, **21** (2024), 101772. https://doi.org/10.1016/j.rineng.2024.101772
9. A. Jan, M. Mushtaq, M. Hussain, Heat transfer enhancement of forced convection magnetized cross model ternary hybrid nanofluid flow over a stretching cylinder: non-similar analysis, I*nt. J. Heat Fluid Flow*, **106** (2024), 109302. https://doi.org/10.1016/j.ijheatfluidflow.2024.109302

10. M. Rahman, H. Waheed, M. Turkyilmazoglu, M. S. Siddiqui, Darcy–Brinkman porous medium for dusty fluid flow with steady boundary layer flow in the presence of slip effect, *Int. J. Mod. Phys. B*, **38** (2024), 2450152. https://doi.org/10.1142/S0217979224501522
11. A. Rehman, M. S. Al-Buriahi, H. E. Ali, R. Jan, I. A. Khan, Analytical simulation of Darcy–Forchheimer nanofluid flow over a curved expanding permeable surface, *Fluid Dyn. Res.*, **56** (2024), 065503. https://doi.org/10.1088/1873-7005/ad8b67
12. I. Khan, R. Zulkifli, T. Chinyoka, Z. Ling, M. A. Shah, Numerical analysis of radiative MHD gravity-driven thin film third-grade fluid flow with exothermic reaction and modified Darcy's law on an inclined plane, *Mech. Time-Depend. Mater.*, **29** (2025), 12. https://doi.org/10.1007/s11043-024-09744-x
13. T. Hayat, M. Shafique, A. Tanveer, A. Alsaedi, Magnetohydrodynamic effects on peristaltic flow of hyperbolic tangent nanofluid with slip conditions and Joule heating in an inclined channel, *Int. J. Heat Mass Transf.*, **102** (2016), 54–63. https://doi.org/10.1016/j.ijheatmasstransfer.2016.05.105
14. H. Adun, M. Abid, D. Kavaz, Y. Hu, J. H. Zaini, Optimizing the thermophysical behavior of a novel ternary hybrid nanofluid for energy applications through experimental research, *Heliyon*, **10** (2024), e32728. https://doi.org/10.1016/j.heliyon.2024.e32728
15. S. A. Lone, Z. Raizah, H. Alrabaiah, S. Shahab, A. Saeed, A. Khan, Exploring convective conditions in three-dimensional rotating ternary hybrid nanofluid flow over an extending sheet: A numerical analysis, *J. Therm. Anal. Calorim.*, 2024. https://doi.org/10.1007/s10973-024-13070-2
16. I. Khan, M. W. Ahmed Khan, Artificial neural networking for computational assessment of ternary hybrid nanofluid flow caused by a stretching sheet: Implications of machine-learning approach, *Eng. Appl. Comput. Fluid Mech.*, **18** (2024), 2411786. https://doi.org/10.1080/19942060.2024.2411786
17. T. N. Tanuja, S. Manjunatha, H. S. Migdadi, R. Saadeh, A. Qazza, U. Khan, et al., Leveraging artificial neural networks approach for thermal conductivity evaluation in porous rectangular wetted fins filled with ternary hybrid nanofluid, *J. Radiat. Res. Appl. Sci.*, **17** (2024), 101125. https://doi.org/10.1016/j.jrras.2024.101125
18. H. Kim, Y. Do, S. Ramachandran, M. Sankar, K. Thirumalaisamy, Computational analysis of magnetohydrodynamic ternary-hybrid nanofluid flow and heat transfer inside a porous cavity with shape effects, *Phys. Fluids*, **36** (2024), 082008. https://doi.org/10.1063/5.0222802
19. D. Mohanty, G. Mahanta, S. Shaw, Irreversibility and thermal performance of nonlinear radiative cross-ternary hybrid nanofluid flow about a stretching cylinder with industrial applications, *Powder Technol.*, **433** (2024), 119255. https://doi.org/10.1016/j.powtec.2023.119255
20. A. Z. Ullah, X. Guo, T. Gul, I. Ali, A. Saeed, A. M. Galal, Thin film flow of the ternary hybrid nanofluid over a rotating disk under the influence of magnetic field due to nonlinear convection, *J. Magn. Magn. Mater.*, **573** (2023), 170673. https://doi.org/10.1016/j.jmmm.2023.170673
21. D. Mohanty, G. Mahanta, S. Shaw, R. Katta, Entropy and thermal performance on shape-based 3D tri-hybrid nanofluid flow due to a rotating disk with statistical analysis, *J. Therm. Anal. Calorim.*, **149** (2024), 12285–12306. https://doi.org/10.1007/s10973-024-13592-9
22. M. Faizan, M. Ajithkumar, M. V. Reddy, M. A. Jamal, B. Almutairi, N. A. Shah, J. D. Chung, A theoretical analysis of the ternary hybrid nano-fluid with Williamson fluid model, *Ain Shams Eng. J.*, **15** (2024), 102839. https://doi.org/10.1016/j.asej.2024.102839

23. M. Ramzan, F. Ali, N. Akkurt, A. Saeed, P. Kumam, A. M. Galal, Computational assessment of Carreau ternary hybrid nanofluid influenced by MHD flow for entropy generation, *J. Magn. Magn. Mater.*, **567** (2023), 170353. https://doi.org/10.1016/j.jmmm.2023.170353
24. A. Mishra, S. K. Rawat, M. Yaseen, M. Pant, Development of machine learning algorithm for assessment of heat transfer of ternary hybrid nanofluid flow towards three different geometries: Case of artificial neural network, *Heliyon*, **9** (2023), e21436. https://doi.org/10.1016/j.heliyon.2023.e21453
25. A. Mishra, Analysis of waste discharge concentration in radiative hybrid nanofluid flow over a stretching/shrinking sheet with chemical reaction, *Mech. Time-Depend. Mater.*, **29** (2025), 7. https://doi.org/10.1007/s11043-024-09752-x
26. A. Mishra, Significance of Thompson and Troian slip effects on Fe_3O_4-$CoFe_2O_4$ ethylene glycol-water hybrid nanofluid flow over a permeable plate, *Hybrid Adv.*, **6** (2024), 100262. https://doi.org/10.1016/j.hybadv.2024.100262
27. A. Mishra, Hydrothermal performance of hybrid nanofluid flow over an exponentially stretching sheet influenced by gyrotactic microorganisms: A comparative evaluation of Yamada-Ota and Xue models, *Numer. Heat Transf. Part A Appl.*, 2024, 1–30. https://doi.org/10.1080/10407782.2024.2363496
28. G. Ramasekhar, F. Mebarek-Oudina, S. Suneetha, H. Vaidya, P. D. Selvi, Computational simulation of Casson hybrid nanofluid flow with Rosseland approximation and uneven heat source/sink, *Int. J. Thermofluids*, **24** (2024), 100893. https://doi.org/10.1016/j.ijft.2024.100893
29. N. Z. Basha, F. Mebarek-Oudina, R. Choudhari, H. Vaidya, B. Hadimani, K. V. Prasad, et al., Thermal radiation effect on mixed convective Casson fluid flow over a porous stretching sheet with variable fluid properties, *J. Adv. Res. Fluid Mech. Therm. Sci.*, **111** (2023), 1. https://doi.org/10.37934/arfmts.111.1.127
30. I. Chabani, F. Mebarek-Oudina, Convection with Cu-MgO/Water hybrid nanofluid and discrete heating, In: *Mathematical Modelling of Fluid Dynamics and Nanofluid*s, CRC Press, 2023, 495–510.
31. A. Mezaache, F. Mebarek-Oudina, H. Vaidya, Y. Fouad, Heat transfer analysis of nanofluid flow with entropy generation in a corrugated heat exchanger channel partially filled with porous medium, *Heat Trans.*, **53** (2024), 4625–4647. https://doi.org/10.1002/htj.23149
32. L. S. Sundar, E. V. Ramana, M. K. Singh, A. C. Sousa, Thermal conductivity and viscosity of stabilized ethylene glycol and water mixture Al_2O_3 nanofluids for heat transfer applications: An experimental study, *Int. Commun. Heat Mass Trans.*, **56** (2014), 86–95. https://doi.org/10.1016/j.icheatmasstransfer.2014.06.009
33. Y. Zhang, N. Shahmir, M. Ramzan, H. A. S. Ghazwani, M. Y. Malik, Comparative analysis of Maxwell and Xue models for a hybrid nanofluid film flow on an inclined moving substrate, *Case Stud. Therm. Eng.*, **28** (2021), 101598. https://doi.org/10.1016/j.csite.2021.101598
34. Y. Zhang, N. Shahmir, M. Ramzan, H. A. S. Ghazwani, M. Y. Malik, Comparative analysis of Maxwell and Xue models for a hybrid nanofluid film flow on an inclined moving substrate, *Case Stud. Therm. Eng.*, **28** (2021), 101598. https://doi.org/10.1016/j.csite.2021.101598
35. A. M. Galal, A. Akgül, S. A. Idris, S. Formanova, T. K. Ibrahim, M. K. Hassani, et al,, The performance evolution of Xue and Yamada-Ota models for local thermal non equilibrium effects on 3D radiative Casson trihybrid nanofluid, *Sci. Rep.*, **15** (2025), 7325. https://doi.org/10.1038/s41598-025-87257-4

36. M. Y. Rafiq, A. Sabeen, A. U. Rehman, Z. Abbas, Comparative study of Yamada-Ota and Xue models for MHD hybrid nanofluid flow past a rotating stretchable disk: Stability analysis, *Int. J. Numer. Methods Heat Fluid Flow*, **34** (2024), 3793–3819. https://doi.org/10.1108/HFF-01-2024-0060
37. T. Maryam, U. Ahmad, G. Rasool, M. Ashraf, T. Sun, I. Razzaq, Numerical study of the thermal performance of the combined effect of solar energy and variable density around a laminar vertical jet, *Case Stud. Therm. Eng.*, **56** (2024), 104275. https://doi.org/10.1016/j.csite.2024.104275
38. J. C. Mollendorf, B. Gebhart, Thermal buoyancy in round laminar vertical jets, *Int. J. Heat Mass Trans.*, **16** (1973), 735–745. https://doi.org/10.1016/0017-9310(73)90087-2
39. T. Mogi, S. Horiguchi, Experimental study on the hazards of high-pressure hydrogen jet diffusion flames, *J. Loss Prev. Proc. Ind.*, **22** (2009), 45–51. https://doi.org/10.1016/j.jlp.2008.08.006
40. S. Siddiqa, S. Asghar, M. A. Hossain, Radiation effects in mixed convection flow of a viscous fluid having temperature-dependent density along a permeable vertical plate, *J. Eng. Phys. Thermophy.*, **85** (2012), 339–348. https://doi.org/10.1007/s10891-012-0658-1
41. H. Maurer, C. Kessler, Identification and quantification of ethylene glycol and diethylene glycol in plasma using gas chromatography-mass spectrometry, *Arch. Toxicol.*, **62** (1988), 66–69. https://doi.org/10.1007/BF00316260
42. A. Mariano, M. J. Pastoriza-Gallego, L. Lugo, A. Camacho, S. Canzonieri, M. M. Piñeiro, Thermal conductivity, rheological behaviour and density of non-Newtonian ethylene glycol-based SnO_2 nanofluids, *Fluid Phase Equilib.*, **337** (2013), 119–124. https://doi.org/10.1016/j.fluid.2012.09.029
43. S. Mukhopadhyay, P. R. De, K. Bhattacharyya, G. C. Layek, Casson fluid flow over an unsteady stretching surface, *Ain Shams Eng. J.*, **4** (2013), 933–938. https://doi.org/10.1016/j.asej.2013.04.004
44. M. Y. Rafiq, A. Sabeen, A. U. Rehman, Z. Abbas, Comparative study of Yamada-Ota and Xue models for MHD hybrid nanofluid flow past a rotating stretchable disk: stability analysis, *Int. J. Numer. Methods Heat Fluid Flow*, **34** (2024), 3793–3819. https://doi.org/10.1108/HFF-01-2024-0060

AIMS Press